ELEMENTA
Science of the Anthropocene

Fang, Y-C, et al. 2026. Upper-ocean variability in the Amundsen Basin of the Arctic Ocean during early winter: Insights from the MOSAiC expedition. *Elem Sci Anth*, 14: 1. DOI: https://doi.org/10.1525/elementa.2023.00095

RESEARCH ARTICLE

Upper-ocean variability in the Amundsen Basin of the Arctic Ocean during early winter: Insights from the MOSAiC expedition

Ying-Chih Fang[1,2,*], Benjamin Rabe[2], Ivan Kuznetsov[2], Mario Hoppmann[2], Sandra Tippenhauer[2], Julia Regnery[2], Hailun He[3], and Tao Li[4,5]

Wintertime observations in the central Arctic Ocean are sparse. We report a unique early winter data set containing atmospheric, hydrographic, and ocean velocity observations obtained during the first leg of the Multidisciplinary drifting Observatory for the Study of Arctic Climate (MOSAiC) expedition, with sea ice concentration at nearly 100%. One storm and four other periods of strong wind were encountered during the drift. This work focuses on the impact of the storm on oceanic variability in the upper 200 m. Variable oceanic surface mixed layers and pervasive horizontal density gradients were observed in the upper 100 m. Several anomalously large horizontal density gradients which lasted 1–2 days can be related to intrahalocline eddies. The nearly mixed upper 20-m water column and the deeper heavily stratified layer belonged to two separate dynamical regimes and appeared unaffected by the storm. Signatures of forced currents due to high ice drift speeds and velocity maxima resulting from intrahalocline eddies were seen above and below the base of the mixed layer, respectively. Near-inertial internal waves (NIWs) were detected among ice floes underneath the base of the mixed layer and were prevalent in the upper 100 m. Some NIWs were observed at depths deeper than 100 m with downward energy propagation. These results imply NIWs were generated at the surface. The single storm potentially injected half the overall near-inertial energy into the mixed layer, underlining the role of storm systems in the Arctic winter. Our results suggest that internal ice stress dampens momentum transfer from wind to the upper ocean, rendering wind forcing insufficient to erode preexisting stratification under full sea ice cover. This dampening contributes to the persistent thermohaline gradients observed. Instead, sea ice moving coherently in response to the winds acts as the main surface forcing driving upper-ocean processes such as NIWs.

Keywords: Winter observations, Central Arctic Ocean, Sea ice, Upper-ocean variability, Storm impact

1. Introduction

The Arctic has been recognized as a region of persistent warming in a trend that appears to be irreversible. The regional magnitude of the warming exceeds that of the global average, a feature called Arctic amplification (Alexeev et al., 2012; Rantanen et al., 2022). The rising air temperature in the Arctic (Stroeve et al., 2018) along with an increasing heat flux through the subpolar seas (Woodgate et al., 2010; Rudels et al., 2015) delays freeze-up and ice growth in winter (Shimada et al., 2006; Kwok and Untersteiner, 2011), resulting in the observed Arctic sea ice decline. The loss of Arctic sea ice has a profound impact on the regional and even global climate variability and energy balance, fundamentally influencing both the atmosphere and the ocean through broader temporal and spatial scales. Sea ice loss has been linked to changes in surface albedo (Kwok and Untersteiner, 2011) and anomalous weather patterns (Jaiser et al., 2016), such as increasing winter cyclones (Rinke et al., 2017) and extremely cold (Tang et al., 2013) or warm (Graham et al., 2017) atmospheric events. As a result of the diminishing Arctic sea ice cover, atmospheric forcing on the ocean and influences from sub-Arctic seas can be expected to become stronger. The more influential role of atmospheric forcing will result in mixing in the water column and favor potential ventilation of the deep and salty (salinity > 34.5) Atlantic Water (AW) which is warmer than the local

[1] Department of Oceanography, College of Marine Sciences, National Sun Yat-sen University, Kaohsiung, Taiwan
[2] Alfred-Wegener-Institut Helmholtz-Zentrum für Polar- und Meeresforschung, Bremerhaven, Germany
[3] State Key Laboratory of Satellite Ocean Environment Dynamics, Second Institute of Oceanography, Ministry of Natural Resources, Hangzhou, China
[4] College of Oceanic and Atmospheric Sciences, Ocean University of China, Qingdao, China
[5] Pilot National Laboratory for Marine Science and Technology, Qingdao, China
* Corresponding author:
Email: ying-chih.fang@mail.nsysu.edu.tw

freezing temperature. This phenomenon has been recorded observationally in the eastern Eurasian Basin, with the term Atlantification (Polyakov et al., 2017; Polyakov et al., 2025) being used for this introduction of extra heat from AW into the near-freezing upper ocean, impeding winter sea ice development. The implication is that heat release from the interior could disturb the sea ice lifecycle in the Arctic Ocean dramatically.

The Arctic Ocean hosts a variety of dynamical processes that may differ substantially from those of midlatitude oceans (Timmermans and Winsor, 2013), such as surface frontal systems, mesoscale eddies (Timmermans et al., 2008; Manucharyan and Timmermans, 2013) at different depth ranges (Zhao and Timmermans, 2016), and internal wave energy which is relatively weak in these regions (Guthrie et al., 2013). Also, the oceanic mesoscales shrink from 50–100 km at midlatitudes (Smith, 2007) to an order of 10–20 km in the polar seas (Nurser and Bacon, 2014; Timmermans and Marshall, 2020). This shrinkage means that observations with a spatial resolution of less than $O(10)$ km, made to investigate these processes and their coupling, need to be favored when designing an observational program in the Arctic Ocean. Implementing this type of observational platform is challenging in the winter Arctic Ocean, making the data that result from them particularly valuable for Arctic research. One such program was the Surface Heat Budget of the Arctic Ocean experiment (SHEBA; see Uttal et al., 2002), which pioneered paradigm-integrating multidisciplinary measurements of the coupled atmosphere-ice-ocean system over one year, though the single ice camp used in SHEBA was insufficient to resolve horizontal variability around the occupied ice floe.

In seasonal variation, sea ice cover becomes more consolidated and less mobile in winter. Martini et al. (2014) analyzed yearlong data from moorings off the Beaufort continental slope and found that >90% sea ice concentration (SIC) in winter effectively reduces surface-forced internal waves. Whether this seasonal pattern of internal wave generation can be found in the more remote central Arctic Ocean, where winter observations are much sparser, is not clear. Generation of surface-forced internal waves relies on the coupled air-water and ice-water stresses in ice-covered seas. Ice-water stress is usually parameterized by a drag law (Morison et al., 1985; Yang, 2006), but local validation of the drag law against other in situ measurements has not received much attention. However, the unique data set derived from observations of the Multidisciplinary drifting Observatory for the Study of Arctic Climate (MOSAiC) expedition has now allowed us to examine ice-water stress parameterization and internal wave wavefield activity in the fully ice-covered central Arctic Ocean in winter.

The MOSAiC expedition took place from late September 2019 to early October 2020 onboard the German icebreaker R/V *Polarstern* (Knust, 2017). The resulting data were collected by different groups in a multidisciplinary manner, and comprised traditional ship-based and nearby ice-based observations obtained on the main ice floe where R/V *Polarstern* was moored. This setting is also called the MOSAiC Central Observatory (CO; Nicolaus et al., 2022; Rabe et al., 2022; Shupe et al., 2022; Fong et al., 2024). The CO observations were uniquely augmented by a buoy array that included various types of spatially separated autonomous sensor packages deployed on surrounding ice floes within a radius of about 40 km from the ship. The network of autonomous sensors is herein referred to as Distributed Network (DN; see Rabe et al., 2024). With the DN, investigating spatial gradients of parameters and features around the main ice floe became possible (Kuznetsov et al., 2024; Watkins et al., 2024; Quintanilla-Zurita et al., 2026). In this article, we closely examined the hydrographic and velocity fields of the upper 200-m water column in the expanse of ocean monitored by the DN during the period October 28–December 12, 2019 (Leg 1 of MOSAiC; **Figure 1**). We focused on the interactions and response of the coupled atmosphere-ice-ocean system to a storm and four selected strong wind events which passed through the MOSAiC domain during the period. This article is organized as follows. The data and associated analysis techniques are explained in Sections 2 and 3, and results and discussion follow in Section 4. We conclude the article with findings and implications in Section 5.

2. Data

2.1. Hydrographic observations from Central Observatory

Two Sea-Bird 911-plus conductivity/temperature/depth (CTD) systems were used during MOSAiC. A ship-based CTD system containing a 24-position rosette of 12-liter Niskin bottles was lowered through an ice hole next to the vessel, and is referred to as *Polarstern*-CTD or "PS-CTD" in this article. A second, smaller CTD system with a 12-position rosette of 5-liter Niskin bottles was deployed in another ice hole inside a shelter on the ice at about 250 m distance from the vessel. We call this platform the Ocean City-CTD or "OC-CTD." Water depths during Leg 1 were approximately 4400 m. The PS-CTD was able to obtain full-depth profiles, while OC-CTD measurements were constrained by its smaller winch which only reached as deep as 1000 m. PS-CTD and OC-CTD data on Leg 1 have been archived in the data publisher Pangaea (Felden et al., 2023) and can be found in Tippenhauer et al. (2023a) and Tippenhauer et al. (2023b), with in situ temperature (in °C) and salinity (in practical salinity scale) accuracies of 0.002°C and 0.004, respectively. Raw CTD data were used to derive 1-dbar averaged profiles of potential temperature (θ, in °C), potential density anomaly (σ_θ, in kg m^{-3}), and buoyancy frequency (N, in cph). This article examines 18 PS-CTD casts, three of which reached 10–15 m above the seafloor, and an additional 29 OC-CTD casts spanning 120–1000 m in depth (**Figure 2a**).

2.2. Hydrographic observations from Distributed Network

The DN contained eight M sites (**Figure 2a**), which hosted smaller autonomous buoys, and three L sites (sites L1, L2, and L3; **Figure 2b**), where the most comprehensive sensor

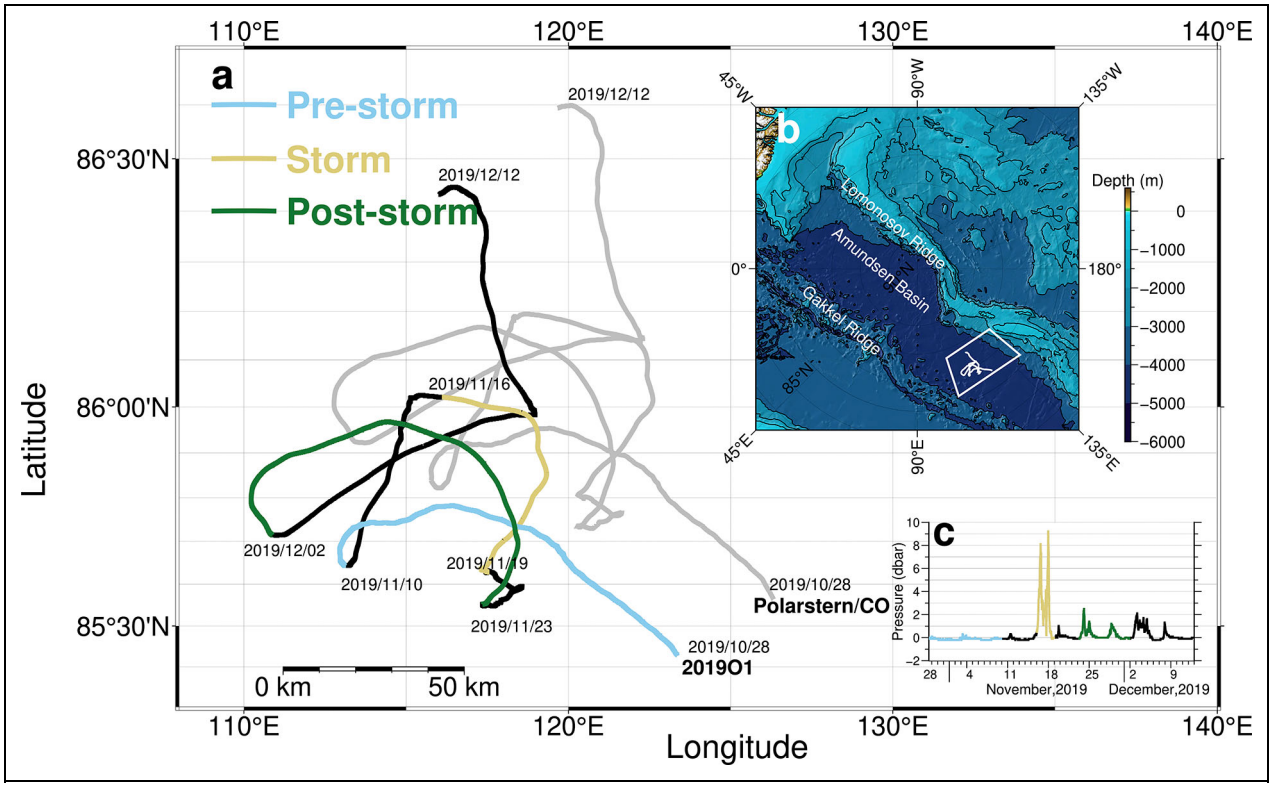

Figure 1. Drift trajectories during the MOSAiC expedition. (a) The gray line denotes the drift trajectory of R/V *Polarstern* during October 28–December 12, 2019, on Leg 1 of the MOSAiC expedition. The colored line shows the trajectory of one Salinity-Ice-Tether buoy, labeled 2019O1, with three different colors (blue, gold, and green) defining specific periods with respect to the passage of the storm: pre-storm, October 28–November 10; storm, November 16–19; and post-storm, November 23–December 2. (b) Regional map showing the study area (white box) in the Arctic Ocean. The white line is the drift trajectory of R/V *Polarstern*. (c) Pressure difference relative to the first measurement from October 28, 2019, derived from the CTD sensor package at the nominal depth of 100 m of Buoy 2019O1. The different colors denote the same periods as defined for the trajectory shown in (a).

Table 1. Nominal depths of conductivity-temperature-depth (CTD) data availability from Salinity-Ice-Tether buoys

	Nominal Depths (m)	
Buoy ID	**CTD Data Available**	**CTD Data Not Available**
2019O1	10, 20, 50, 75, 100	N/A
2019O3	10, 20, 75, 100	50
2019O4	10, 20, 50, 100	75
2019O5	10, 50, 100	20, 75
2019O6	10, 20, 50, 75, 100	N/A

packages were deployed (Rabe et al., 2024). A Woods Hole Oceanographic Institution (WHOI) Ice-Tethered Profiler (ITP; Krishfield et al., 2008) was deployed at each L site. The ITP contained one surface unit transmitting GPS location and raw data back to the land server and one under-ice profiling CTD system that conducted two one-way temperature and salinity profiles at 7–750 m depths separated by 6 hours each day. To generate time series of its representative Leg 1 surface mixed layer depths, we mostly used the final processed 1-m averaged data from the ITP at site L1 (Toole et al., 2016; see data section of ITP 111). We computed potential temperature and potential density anomaly for subsequent analyses.

One autonomous Salinity-Ice-Tether (SIT) buoy measuring upper-ocean temperature and salinity was deployed individually at each M site. These eight SIT buoys are identified as 2019O1, 2019O2, . . . , to 2019O8. Each SIT buoy consisted of a floatable surface unit housing the electronics, battery, and iridium modem, attached to a 100-m long inductive wire cable stabilized with a 10 kg terminal weight. Five Sea-bird SBE37-IMP MicroCAT CTDs were clamped onto the cable at nominal depths of 10, 20, 50, 75, and 100 m. The buoy transmitted seawater temperature, conductivity, and instrument pressure, along with GPS position and surface temperature at 10-minute intervals. Unfortunately, three (2019O2, 2019O7, and 2019O8) of the SIT buoys were lost due to ice deformation before November 13, 2019. Only data collected by the remaining five buoys 2019O1, 2019O3, 2019O4, 2019O5, and 2019O6 (**Figure 2a**; **Table 1**) have been analyzed in this article. The relative separations of these five SIT buoys varied from 20 km to 70 km. Outliers in the data were identified by inspection

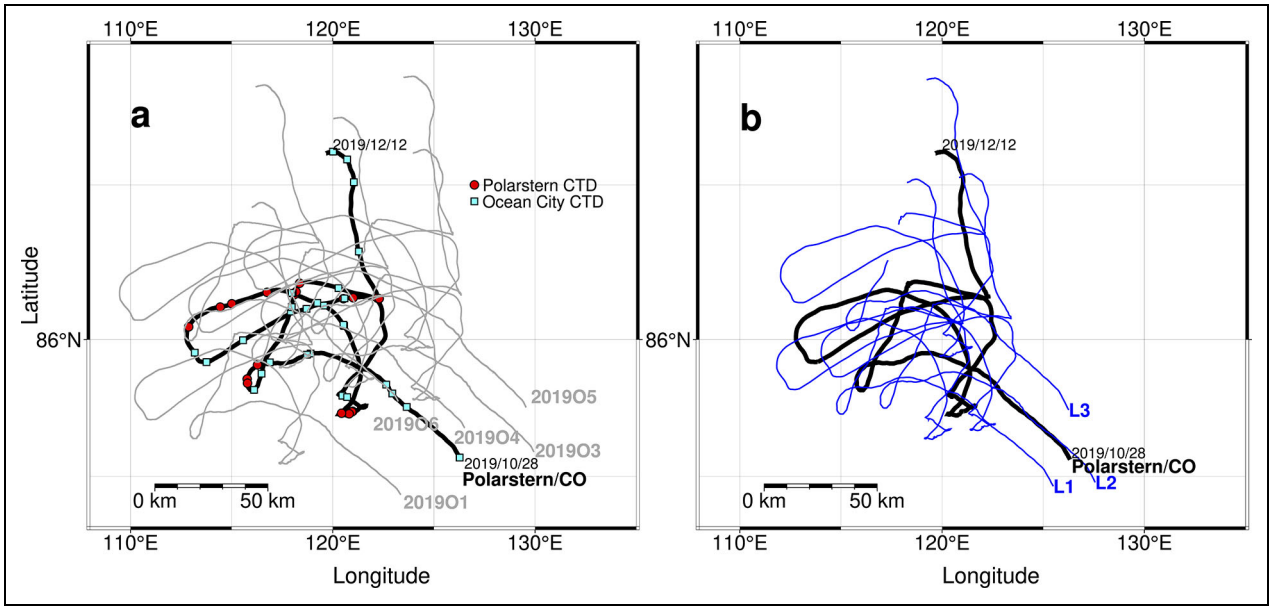

Figure 2. Overview of the drift during Leg 1. (a) Drift trajectories of R/V *Polarstern* (black) and five Salinity-Ice-Tether buoys of the Distributed Network (gray) from October 28–December 12, 2019. The ID numbers of the buoys are labeled. Red circles and cyan squares denote CTD casts from R/V *Polarstern* and Ocean City, respectively. (b) Drift trajectories of the three L sites (L1, L2, and L3, blue), with the drift trajectory of R/V *Polarstern* (black).

and removed. The estimated accuracy of the MicroCats is 0.002°C for temperature, 0.003 for salinity, and 0.1 dbar for pressure. We also computed potential temperature and potential density anomaly for these buoys. An alternative version of the SIT data set had been published by Hoppmann et al. (2022a). It merged the transmitted and internally stored data of each MicroCAT CTD resulting in better vertical (0.02 dbar) and temporal (2-minute) resolutions. Using this alternative version of the SIT data set does not alter the results of this article. Primarily Buoy 2019O1 is analyzed here because its time series is the most complete. The data from the SIT buoys presented in Hoppmann et al. (2022a) are archived in Hoppmann et al. (2022b).

2.3. Meteorological measurements

Air temperature, barometric pressure, and wind velocity data from the meteorological observatory onboard R/V *Polarstern* were used to determine meteorological conditions and atmospheric forcing throughout the study period. Air temperature and barometric pressure sensors were located at 29 m and 16 m above the water level, respectively. Winds were measured by a Thies Clima ultrasonic anemometer at a height of 39 m above the water level. Measurements were checked onboard by the designated operator and quality-controlled 1-minute averaged data (Schmithüsen, 2021) were derived before archiving by the data publisher Pangaea. To ensure that winds measured at a height of 39 m were representative of the surface forcing (e.g., of 10-m-high winds), we also checked wind measurements collected by Team Atmosphere from the wind tower at the "Met City" of the MOSAiC CO. The processed 10-minute averaged wind velocity data (see Cox et al., 2023) at 2 m, 6 m, and 10 m heights were used. These wind data were then hourly averaged for subsequent analyses.

2.4. Measurements of ocean currents and under-ice frictional stress

Horizontal upper-ocean current velocities during the drift were determined from a ship-based RDI Ocean Surveyor 150-kHz Acoustic Doppler Current Profiler (SADCP), as archived by the data publisher Pangaea (Tippenhauer and Rex, 2020). From these data, we constructed 8-m bin size, hourly averaged two-dimensional absolute currents with zonal (u) and meridional (v) components in the 25–200 m depths.

However, there were other ADCPs on the Autonomous Ocean Flux Buoys (AOFBs; see Shaw et al., 2008) at the MOSAiC CO and three L sites of the DN. These ADCPs collected upper-ocean currents between 4 m and 70 m depths at 2-m resolution. We used the processed, ADCP-derived two-dimensional absolute ocean currents from the AOFBs at CO (sampling interval of 2 hours; Stanton and Shaw, 2023a), L1 (sampling interval of 3 hours; Stanton and Shaw, 2023b), and L3 (sampling interval of 2 hours; Stanton and Shaw, 2023c). The ADCP from the L2 AOFB had a very shallow (<10 m) depth coverage during Leg 1 and thus was not considered here.

The AOFBs were equipped with an eddy correlation flux package sensor at 5 m depth which directly measured the covariance of fluctuating vertical velocity (w') with fluctuating horizontal velocity (u' or v'). This information is analogous to vertical transfer of momentum fluxes and can be used directly to infer the frictional stress at 5 m depth (Shaw et al., 2008). We used the processed covariance products from the AOFB at L1 (Stanton and

Shaw, 2023b) at 3-hour resolution because they had better temporal coverage.

2.5. Sea ice concentration data

Sea ice cover was measured with a recently developed SIC product (Ludwig et al., 2019; Ludwig et al., 2020) that merges thermal infrared data of the Moderate Resolution Imaging Spectroradiometer (MODIS) and passive microwave measurements of the Advanced Scanning Microwave Radiometer 2 (AMSR2). The MODIS-AMSR2 SIC has a spatial resolution of 1 km and updates at daily intervals. We retrieved the along-track SIC at the nearest grid point from the R/V *Polarstern*. The averaged SIC was about 99.6% (with a standard deviation of 0.57%) during the 46-day-long study period.

3. Methods

3.1. Defined tracks before and after the storm

A storm system struck the study area during November 16–19, 2019. The individual CTDs on the tether of Buoy 2019O1, for instance, exhibited substantial vertical displacements (about 10 dbar; **Figure 1c**) during this period, presumably as a result of the accompanying increased ice drift velocities. This occurrence motivated an examination of the impact of the storm on the ice-covered ocean below. To aid in analysis, we sectioned the storm timeline into three periods: November 16–19 for the storm itself (see the gold "storm" track in **Figure 1a**); and for purposes of evaluating horizontal variability, the two periods before and after the storm, October 28–November 10 (the blue "pre-storm" track in **Figure 1a**) and November 23–December 1 (the green "post-storm" track in **Figure 1a**), during which the SIT buoy trajectory remained relatively straight.

3.2. Analysis of horizontal wavenumber spectra

CTD data from Buoy 2019O1 while on the pre-storm and post-storm tracks were used to compute horizontal wavenumber spectra of σ_θ and determine if their slopes hinted at the dynamics behind them (Dugan et al., 1986; Callies and Ferrari, 2013; Callies et al., 2015; Mackinnon et al., 2016). We first linearly interpolated the along-track observations of σ_θ at the five nominal depths from SIT buoy 2019O1 onto uniform grids at 100 m separations. Then, horizontal wavenumber spectra of σ_θ along the two tracks were computed from these uniformly gridded density observations. The spectra were averaged using a Hamming window with 50% overlap, providing 11 equivalent degrees of freedom (Emery and Thomson, 1997). To examine whether the spectra varied due to passage of the storm, spectral slopes were computed using least-square fit to the spectra in the wavenumber range of 0.1–5 cpkm. Note that the first baroclinic Rossby radius locally is about 10 km (Nurser and Bacon, 2014), which is the inverse of 0.1 cpkm.

3.3. Computation of surface mixed layer depth

We followed Timmermans et al. (2012) in examining surface mixed layer depth (MLD) by defining critical density differences ($\Delta\sigma_\theta$) of 0.01 kg m^{-3} and 0.2 kg m^{-3} from the shallowest measurement of the L1 ITP data. In a nearly mixed water column, both density difference criteria should yield two similar MLDs, while a mismatch between the MLDs suggests the existence of a weakly stratified barrier layer below a mixing layer. We examined mismatches in the record to infer restratification in the upper ocean. The computed MLDs were then daily-averaged before making a 46-day-long time series.

3.4. Computation of wind factor

In this article, $\vec{U}^{\text{ship}}_{\text{wind}}$ denotes the two-dimensional winds measured at 39 m height from R/V *Polarstern*. In order to check its representativeness of the near-surface winds, we examined measured wind speeds at 2, 6, and 10 m heights at Met City and calculated the regression on the $\left|\vec{U}^{\text{ship}}_{\text{wind}}\right|$ reading. The coefficients of determination range was 0.84–0.92, with the highest being with the recordings at a height of 10 m, $\left|\vec{U}^{10}_{\text{wind}}\right|$. This procedure yields a linear relationship between $\left|\vec{U}^{10}_{\text{wind}}\right|$ and $\left|\vec{U}^{\text{ship}}_{\text{wind}}\right|$ by

$$\left|\vec{U}^{10}_{\text{wind}}\right| = -0.1558 + 0.8050\left|\vec{U}^{\text{ship}}_{\text{wind}}\right| \quad (1)$$

As wind measurements at Met City were disabled during the storm's passage, November 16–19, we generated a new complete time series for $\left|\vec{U}^{10}_{\text{wind}}\right|$ with Equation 1, using input from $\left|\vec{U}^{\text{ship}}_{\text{wind}}\right|$. On the basis of this time series, wind factor, a measure of sea ice response to wind forcing, with a larger factor suggesting more mobile sea ice drift, was calculated according to Equation 2,

$$\text{Wind factor} = \left|\vec{U}_{\text{ice}}\right| / \left|\vec{U}^{10}_{\text{wind}}\right| \quad (2)$$

where $\vec{U}_{\text{ice}}$ is two-dimensional horizontal surface ice drift velocity, calculated by the temporal differences of the GPS position of SIT buoy 2019O1, and $\vec{U}^{10}_{\text{wind}}$ is as above.

3.5. Near-inertial fit

Examining the time series of $\vec{U}_{\text{ice}}$, we found episodic oscillations occurring about every 12 hours, suggesting near-inertial oscillation in the sea ice drift. We followed the methodology of Rainville and Woodgate (2009) and Martini et al. (2014) using a harmonic fit at the local inertial frequency *f*. A cosine wave with a frequency *f* was fit to the *u* and *v* components of $\vec{U}_{\text{ice}}$ in a sliding 1.5-day window at hourly intervals to extract near-inertial velocities.

3.6. Analysis of near-inertial internal waves

Applying rotary spectral analysis in time (Gonella, 1972; Emery and Thomson, 1997) onto the SADCP data revealed stronger clockwise spectra with an energy peak around the local inertial frequency (not shown). This result suggests the existence of near-inertial internal waves (NIWs) in the upper 200 m water column. The steps taken processing the SADCP data to characterize the NIWs are explained as follows. We first applied the near-inertial fit technique (Section 3.5) to the SADCP data. This procedure

removes mesoscale eddy signals. As the amplitude and wavenumber of internal waves will be adjusted due to the variable stratification, we applied the Wentzel–Kramers–Brillouin (WKB) scaling (Leaman and Sanford, 1975) to minimize this effect. The SADCP velocity data were multiplied by a factor of $[N(z)/N_0]^{1/2}$ (Alford et al., 2012; Kawaguchi et al., 2019), where N_0 is a chosen reference buoyancy frequency of 3 cph, here, based on observed stratification for the upper 200 m. We then computed vertical shear of the u and v components, u_z and v_z (where subscript z denotes velocity differences in the vertical direction), to better isolate the barotropic semidiurnal tides. If there are features of NIWs in the water column, striped patterns should be manifested in the depth-time plots of u_z and v_z (see also Halle and Pinkel, 2003; Pinkel, 2005; Fer, 2014).

3.7. Ocean surface frictional stress

Two-dimensional surface frictional stress on the ice-covered ocean, $\vec{\tau}^*(\tau_x^*, \tau_y^*)$, where τ_x^* and τ_y^* are components along the zonal and meridional directions, was computed by two different approaches. First, we used the parameterization following Yang (2006) with

$$\vec{\tau}^* = \mathrm{SIC}\vec{\tau}^*_{\text{ice-water}} + (1 - \mathrm{SIC})\vec{\tau}^*_{\text{air-water}} \quad (3)$$

where $\vec{\tau}^*_{\text{ice}-\text{water}}$ and $\vec{\tau}^*_{\text{air}-\text{water}}$ represent ice-water and air-water interfacial stresses, respectively. Averaged SIC during Leg 1 was about 99.6%; thus, wind-driven stress $\vec{\tau}^*_{\text{air-water}}$ is ignored here and Equation 3 may be simplified as

$$\vec{\tau}^* \approx \vec{\tau}^*_{\text{ice-water}} = \rho_w C_{\text{iw}} \left|\vec{U}_{\text{ice}} - \vec{U}_{\text{ocean}}\right| \left(\vec{U}_{\text{ice}} - \vec{U}_{\text{ocean}}\right) \quad (4)$$

where ρ_w is the reference seawater density (1023 kg m^{-3}) and $C_{\text{iw}} = 0.0055$ is the ice-water drag coefficient (Hibler, 1979). Substituting in Equation 4, $\vec{U}_{\text{ice}}$ was computed by the temporal change of the L1 AOFB GPS location. $\vec{U}_{\text{ocean}}$ was represented by the L1 AOFB ADCP velocity measurements at a depth of 15 m.

The second method of computing $\vec{\tau}^*(\tau_x^*, \tau_y^*)$ made use of the measured eddy correlation product of the L1 AOFB flux package sensor at a depth of 5 m (see Section 2.4; Stanton and Shaw, 2023b). According to Equations 5 and 6,

$$\tau_x^* = \rho_w < u'w' > \quad (5)$$

$$\tau_y^* = \rho_w < v'w' > \quad (6)$$

where $<>$ denotes an ensemble mean (McPhee, 2008). Ideally, the values for $\vec{\tau}^*$ using Equation 4 should be similar to those using Equations 5 and 6. To the best of our knowledge, this is the first attempt to compare the surface frictional stress results of these two approaches.

3.8. Mixed layer slab model

The ADCPs of the AOFBs were able to collect velocity measurements within the surface mixed layer. This information can be used to evaluate ocean response to sea ice movement. Following Kawaguchi et al. (2022) and Martini et al. (2014), we employed a theoretical slab model (Pollard and Millard, 1970; D'Asaro, 1985) to investigate the dynamics in the mixed layer with the equations,

$$\frac{du_{\text{ml}}}{dt} - fv_{\text{ml}} = \frac{\tau_x^*}{H_{\text{ref}}\rho_w} - ru_{\text{ml}} \quad (7)$$

$$\frac{dv_{\text{ml}}}{dt} - fu_{\text{ml}} = \frac{\tau_y^*}{H_{\text{ref}}\rho_w} - rv_{\text{ml}} \quad (8)$$

where $\vec{U}_{\text{ml}}(u_{\text{ml}}, v_{\text{ml}})$ is the current vector in the mixed layer with u_{ml} and v_{ml} for zonal and meridional velocity components, respectively, H_{ref} is the reference mixed layer depth, and r is a damping constant that accounts for the loss of mixed layer energy. The slab model with Equations 7 and 8 simulates forced currents in the mixed layer by the surface frictional stress. The value of H_{ref} was set at 30 m based on the ITP data, and r requires $r < f$ (D'Asaro, 1985; Alford, 2001) so that $r = 0.03f$ is chosen here for the optimal simulation results. The forcing terms τ_x^* and τ_y^* were derived from Section 3.7 and hourly interpolated. Finally, we numerically solved u_{ml} and v_{ml} at an hourly time step.

To further evaluate the impact of the storm on the ocean, we followed Alford (2001) in computing the predicted near-inertial energy flux with consideration of a variable MLD at time t by

$$\Pi(\mathrm{MLD}, t) = \frac{H_{\text{ref}}}{\mathrm{MLD}}\Pi(H_{\text{ref}},\ t) \quad (9)$$

where MLD is defined by $\Delta\sigma_\theta$ = 0.01 kg m^{-3} in Section 3.3. $\Pi(H_{\text{ref}},\ t)$ in Equation 9 is computed by

$$\Pi(H_{\text{ref}},\ t) = \vec{\tau}^* \cdot \vec{U}_{\text{ml}} \quad (10)$$

Equation 10 states that $\vec{\tau}^*$ exerts positive energy flux in the mixed layer when $\vec{\tau}^*$ and $\vec{U}_{\text{ml}}$ are oriented in the same direction.

4. Results and discussion

4.1. General environmental conditions during Leg 1

A storm system transiting eastwards from Greenland struck the main ice floe November 16–19, 2019. The observed barometric pressure dropped from 1029 hPa to 992 hPa and was accompanied by an air temperature increase from −15°C to −5.2°C (**Figure 3a**) while the storm was closest to the main ice floe on November 16–17. Rotation of the storm caused a change in wind direction from southwest to north, with a maximum wind speed of 22 m s^{-1} measured on R/V *Polarstern* (see the black vectors and red line in **Figure 3b**). Besides the storm, there were four other strong wind periods with magnitudes greater than 15 m s^{-1} during the periods, November 11–13 (Event 1), November 23–25 (Event 2), November 28–30 (Event 3), and December 2–6 (Event 4). The oceanic conditions and response under these other wind events will be examined separately later.

The wind factor, a measure of ice motion in response to the wind, was generally above 0.02 for winds stronger than 10 m s^{-1}. Note that the anomalous increases of the wind factor, for example on November 2 and December 6, were the result of weak winds during periods of wind relaxation. The largely non-zero wind factor reflects that ice movement was not constrained during Leg 1. The coefficient of determination between wind speed and ice drift

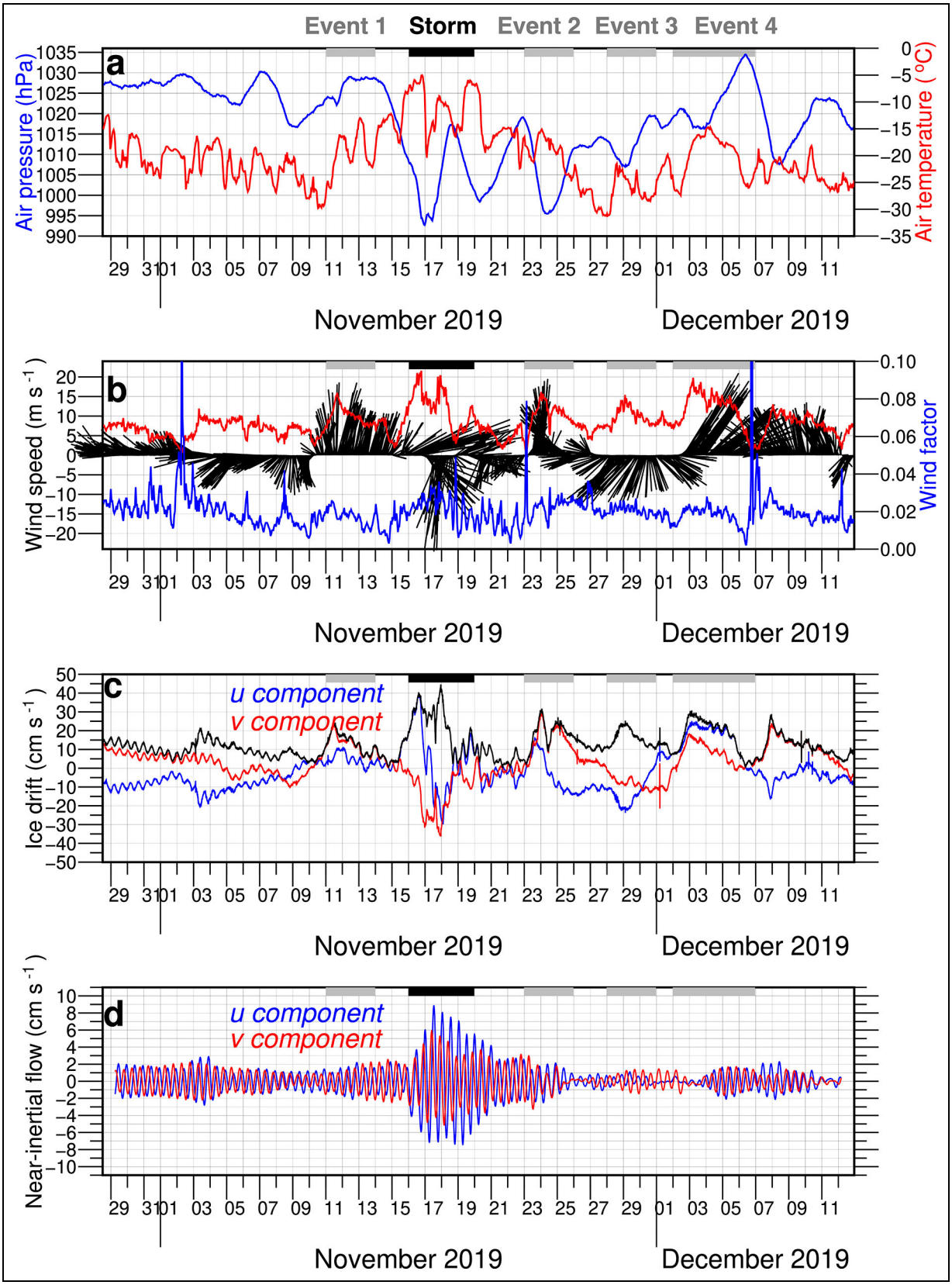

Figure 3. Meteorological measurements and sea ice drift derived from CO and SIT buoy 2019O1. (a) Time series of daily barometric pressure (blue) and air temperature (red) measurements onboard R/V *Polarstern* at Central Observatory (CO). (b) Time series of wind vectors (black), wind speeds (red), and wind factor (blue). (c) Time series of *u* component (blue), *v* component (red), and speeds (black) of sea ice drift derived from Salinity-Ice-Tethered (SIT) buoy 2019O1. (d) Time series of near-inertial *u* component (blue) and *v* component (red) derived from ice drift components in panel (c). At the top of each panel, the storm (black bar) and the four selected strong wind events (gray bars) are indicated.

speed was about 0.77, indicating that sea ice motion was largely coupled with wind activity. This coupling explains the coherent movements of the ice floes of CO and DN (**Figure 2**). The storm led to an increase in ice drift speed to nearly 50 cm s^{-1}, and oscillatory patterns in both u and v components were found in ice drift velocities (**Figure 3c**). This oscillation has a frequency close to f and is interpreted as near-inertial motions caused by wind vector variability. Extracted near-inertial signals from the ice drift velocities (see Section 3.5) were about 2–3 cm s^{-1}, and these near-inertial signals were persistent throughout Leg 1 (**Figure 3d**). The storm amplified the near-inertial velocities up to 10 cm s^{-1}, but they decayed to the pre-storm level of 2–3 cm s^{-1} on November 21. The other four strong wind events did not strengthen near-inertial motions. We attribute this lack of strengthening to wind direction varying less so that the resonant near-inertial response was relatively weak.

4.2. Hydrographic observations during Leg 1

Hydrographic conditions in the upper 500-m ocean based on three full-depth PS-CTD profiles are shown in **Figure 4**. The most prominent feature was the strong salinity-driven stratification above depths of 200 m, with peak buoyancy frequency value of up to 16 cph at 30–50 m depths. The relatively fresh (salinity near 32.6) and near-freezing surface mixed layer was about 30–40 m thick, capping a cold halocline layer where the salinity increased dramatically from 32.7 to 34.3. The Arctic cold halocline layer (Polyakov et al., 2013) was within a depth range of 40–80 m (**Figure 4a**–**c**). The AW layer is characterized by intrusive and interleaving temperatures and is most distinct in the depth range of 200–400 m. During Leg 1, we generally observed relatively warm (about 1.5°C) and salty (near 34.8–34.9) waters of Atlantic origin deeper than 180 m (see their figures 9–10 in Rabe et al., 2022), with three temperature maxima at around 180 m, 250 m, and 330 m. These observations are consistent with previous measurements (Rudels et al., 2015).

The salinity and density data above a depth of 40 m (**Figure 4b** and **c**) indicate that the MOSAiC floe traversed a near-surface frontal zone around 85.7°N (**Figure 1**) separating near-surface waters with salinity of 32.4 (see profiles on November 14 and December 5) from those with a reading of 32.7 (see profile on November 21). Comparing these three profiles suggests that the storm of November 16–19 had little discernible effect on vertical stratification in the area. This suggestion is supported by the θ-S diagram showing 10 minute resolution data of the SIT 2019O1 buoy (**Figure 5**) in connection with the arrival of the storm of November 16–19. The upper two CTDs clamped at depths of 10 m and 20 m show that the waters were near-freezing and the buoy passed over different horizontal density structures (crossing different isopycnals). If the storm had largely stirred and mixed the upper 20 m water column, the data distribution should tend to be concentrated near an isopycnal in the θ-S space, but this is not the case (**Figure 5**). Data from the CTDs at depths of 50 m, 75 m, and 100 m basically follow the typical θ-S diagram of Leg 1 reported in Rabe et al. (2022; their figure 9), and there is no sign showing

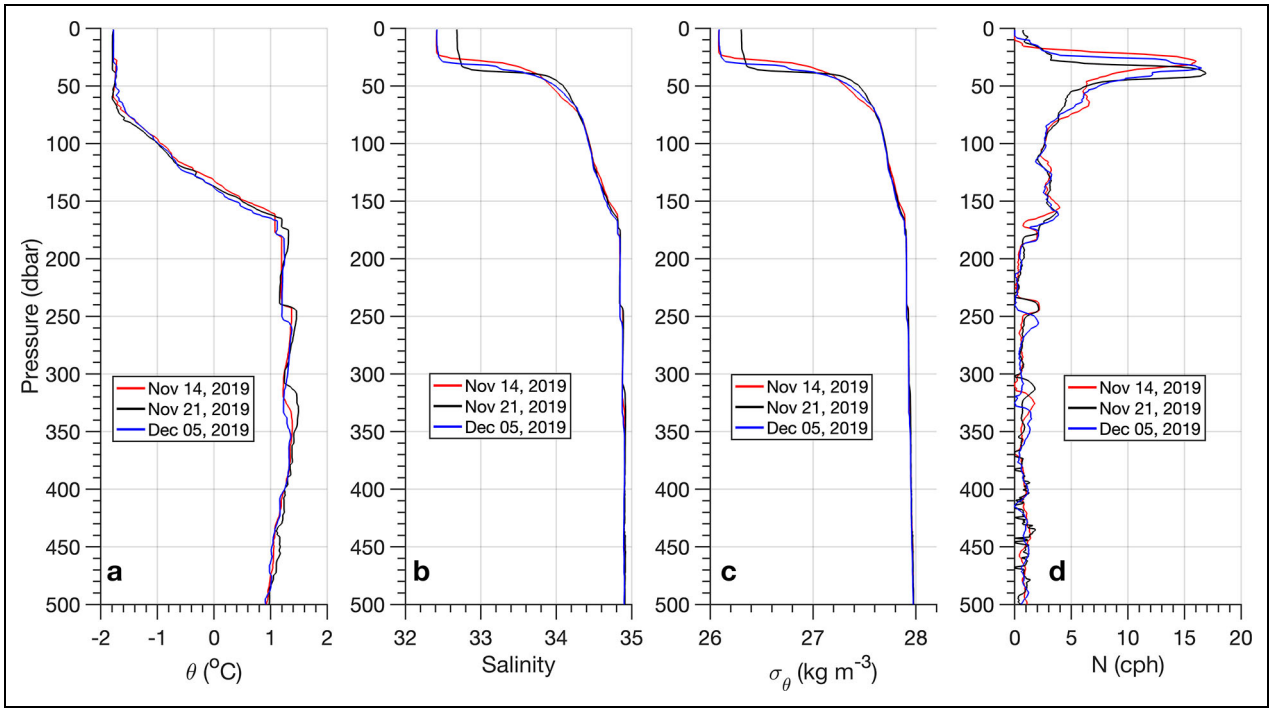

Figure 4. Upper 500 m water profiles from the three full-depth CTD casts near R/V *Polarstern*. Upper 500-m profiles of (a) potential temperature, (b) salinity, (c) potential density anomaly, and (d) buoyancy frequency from three full-depth conductivity-temperature-depth (CTD) casts near R/V *Polarstern* on November 14, 2019 (blue), November 21, 2019 (red), and December 5, 2019 (black).

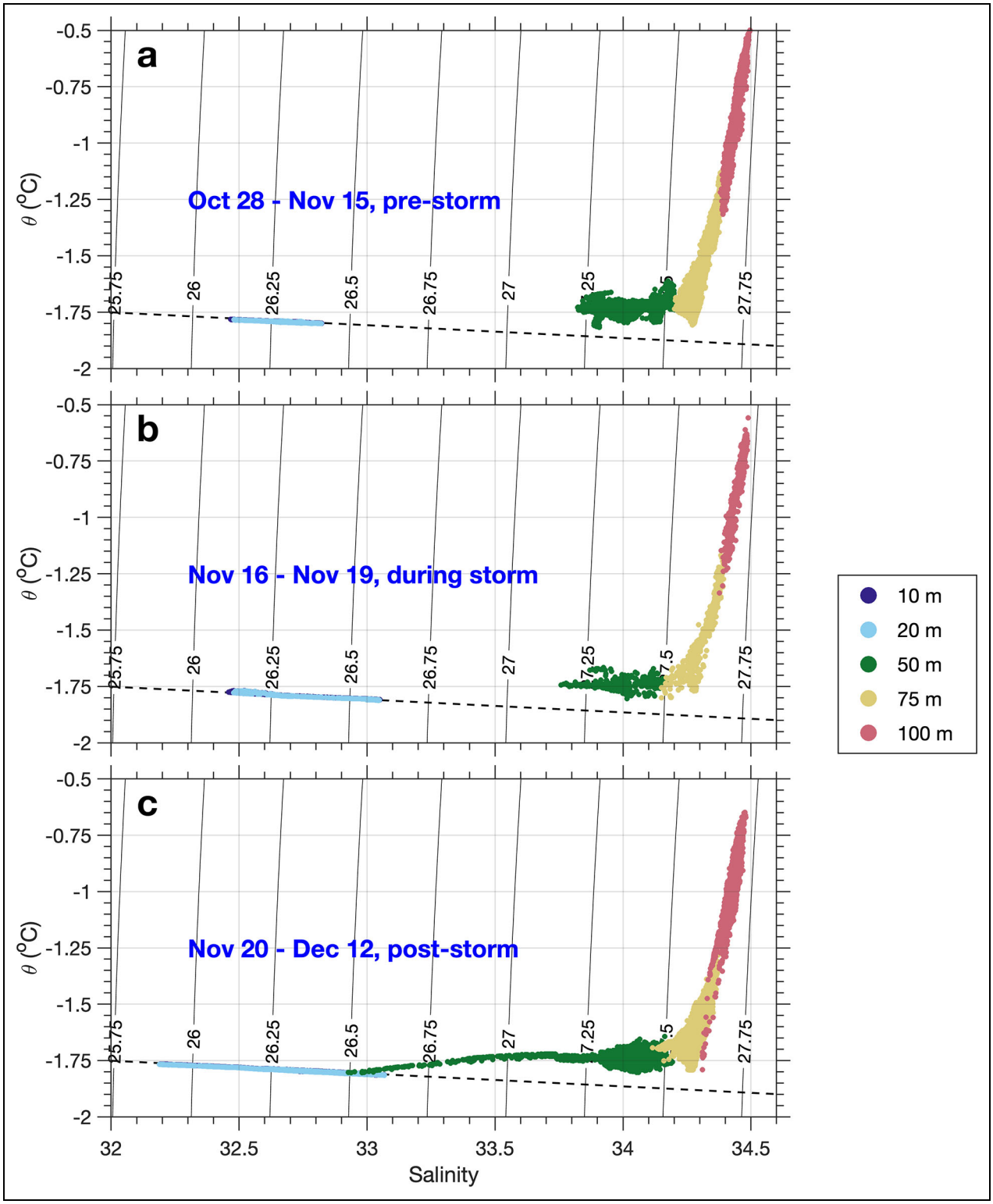

Figure 5. Potential temperature-salinity diagram derived from SIT buoy 2019O1 data. Potential temperature-salinity diagram using data derived from Salinity-Ice-Tethered (SIT) buoy 2019O1 in the (a) pre-storm, (b) storm, and (c) post-storm periods. Dots in different colors denote CTD data at the five nominal depths shown in the legend on the right side of the figure. Thin gray contours denote isopycnal surfaces of σ_θ (in kg m^{-3}), and the black dashed line is the freezing line at sea surface pressure. Note that data at 10 m depth are mostly hidden underneath those at 20 m depth.

waters from the upper pycnocline were upwelled to the shallower depths.

The θ-S diagram shows that the SIT 2019O1 buoy encountered relatively freshwater with salinity of 32.4 above a depth of 20 m in the post-storm period (**Figure 5c**). A near-surface freshwater signal was not observed in **Figure 5a**, but one was present in pre-storm PS-CTD data on November 14 (**Figure 4b**). The

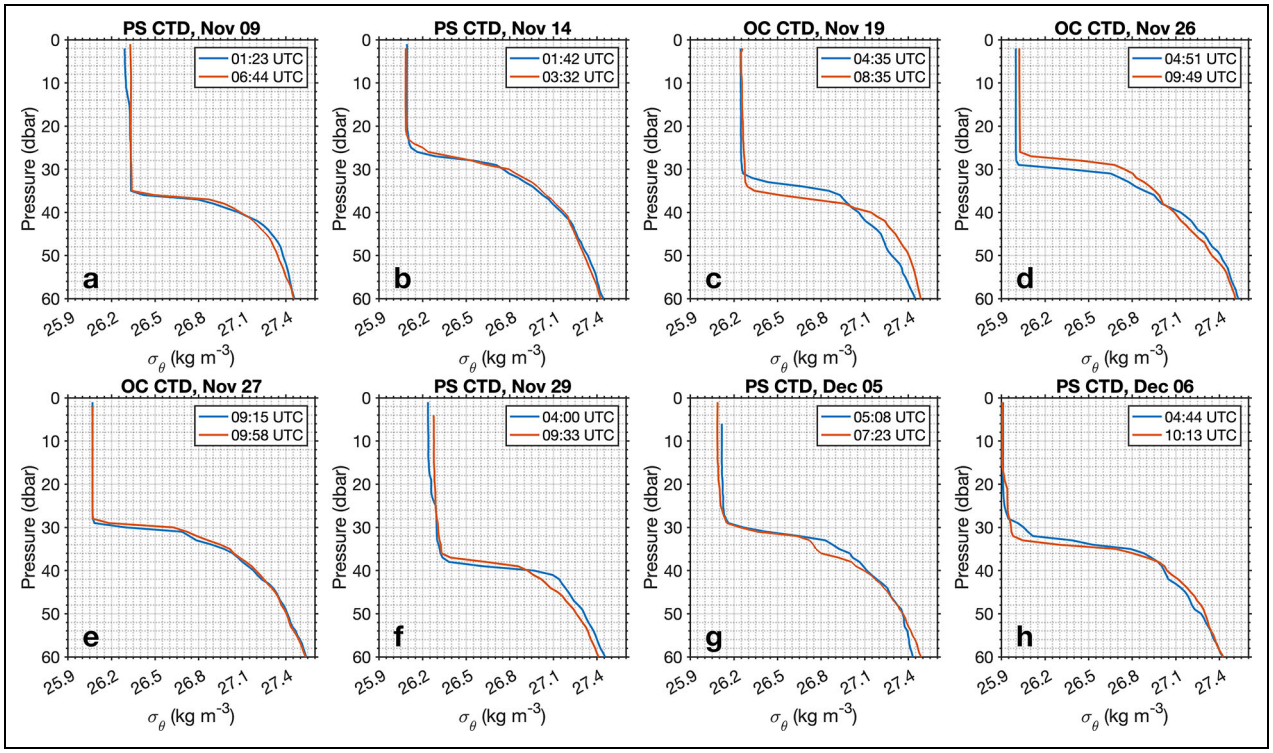

Figure 6. Profiles of potential density anomaly derived from PS-CTD and OC-CTD casts. Consecutive profiles of potential density anomaly from CTD casts near R/V *Polarstern* (PS-CTD) and the Ocean City platform (OC-CTD) on (a) November 9, (b) November 14, (c) November 19, (d) November 26, (e) November 27, (f) November 29, (g) December 5, and (h) December 6. Each day the profiles were 6 hours apart or less, as indicated by the colored lines (blue followed by red).

separation between the CO and the 2019O1 buoy of about 25 km further supports the idea that the MOSAiC floes traversed a near-surface frontal zone. There was a cold pulse recorded by CTDs at 100 m and 50 m depths on December 2. We interpret this cold pulse signal, which was found when examining time series (not shown), as the buoy encountering a lateral advection of waters from the Arctic cold halocline layer.

The L1 ITP collected two hydrographic profiles separated by 6 hours each day. On the other hand, on occasion, near-ship water sampling routines were carried out consecutively, producing PS-CTD or OC-CTD profiles less than 6 hours apart. The MOSAiC floe drifted at $O(10)$ cm s^{-1}, thus we expected these consecutive CTD profiles to reveal submesoscale lateral processes that occur within distances of 5 km. Profile results are shown in **Figure 6**. We focus on the upper 60 m water column, which contains the surface mixed layer and part of the cold halocline layer. A near-surface (<30 m depth) horizontal density gradient can be deduced from the failure of the two profiles there to coincide (**Figure 6a**, **d**, **f**, and **g**). Profiles with a distinct mixed layer are exemplified in **Figure 6d** and **e**. A specific feature of interest is the presence of a weakly stratified barrier layer existing below the upper relatively mixed water column (**Figure 6b**, **c**, and **f–h**). For the profiles on December 6 (**Figure 6h**) as an example, the density weakly increased at depths of around 20–30 m. This feature is reminiscent of the upper-ocean restratification discussed in Timmermans et al. (2012) as the result of frontal slumping.

Next we applied two density difference criteria (see Section 3.3) and constructed the corresponding daily MLDs over time (**Figure 7**). The result shows that the MLDs varied from about 15 m to 45 m in depth. The lack of agreement of the resulting MLDs using $\Delta\sigma_\theta$ =0.01 kg m^{-3} and 0.2 kg m^{-3} is apparent throughout most of Leg 1. This result again argues for the prevalence of a weakly stratified barrier layer under a shallower relatively mixed layer as in the earlier study in the Canada Basin by Timmermans et al. (2012). An implication of not seeing a coordinated MLD evolution is that the MOSAiC floe passed over various near-surface horizontal density gradients above 40 m in depth. Although there were four strong wind events aside from the storm, the MLDs did not always necessarily deepen in response to the wind. We noted that the MLDs appeared to be deeper during the beginning of the storm and other wind events, which were coincident with larger sea ice drift speeds (**Figure 3**), thus suspecting that deepening MLDs during these periods may have been due to shear-related mixing as a result of stronger ice-water stress.

Making use of the 10-minute resolution data from the available SIT buoys, we computed salinity differences between 10 m and 20 m at each time step to shed light on a different aspect of the salinity of near-surface vertical stratification (**Figure 8**). There were times when the vertical salinity difference could be as large as 0.5–0.7 at buoys 2019O3, 2019O4, and 2019O6. These changes in salinity difference typically subsided within 2 days, so the three buoys may have passed over the core of an

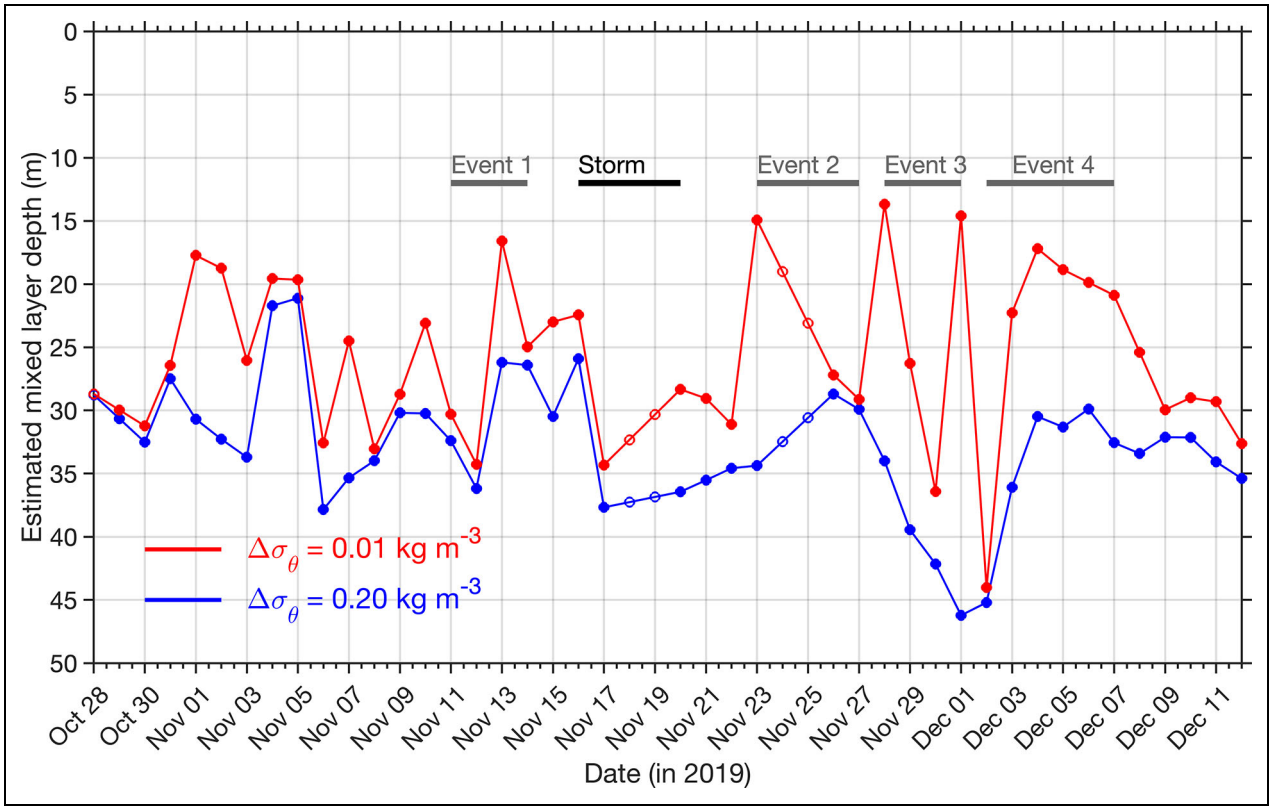

Figure 7. Time series of ITP-estimated mixed layer depth at site L1. Time series of estimated mixed layer depth during Leg 1 using Ice-Tethered Profiler (ITP) data at site L1. Red and blue lines are mixed layer depths using criteria of determinative density differences of 0.01 kg m^{-3} and 0.2 kg m^{-3}, respectively. Open circles denote interpolated values due to missing data. The four selected strong wind events (gray bars) and the storm (black bar) are indicated.

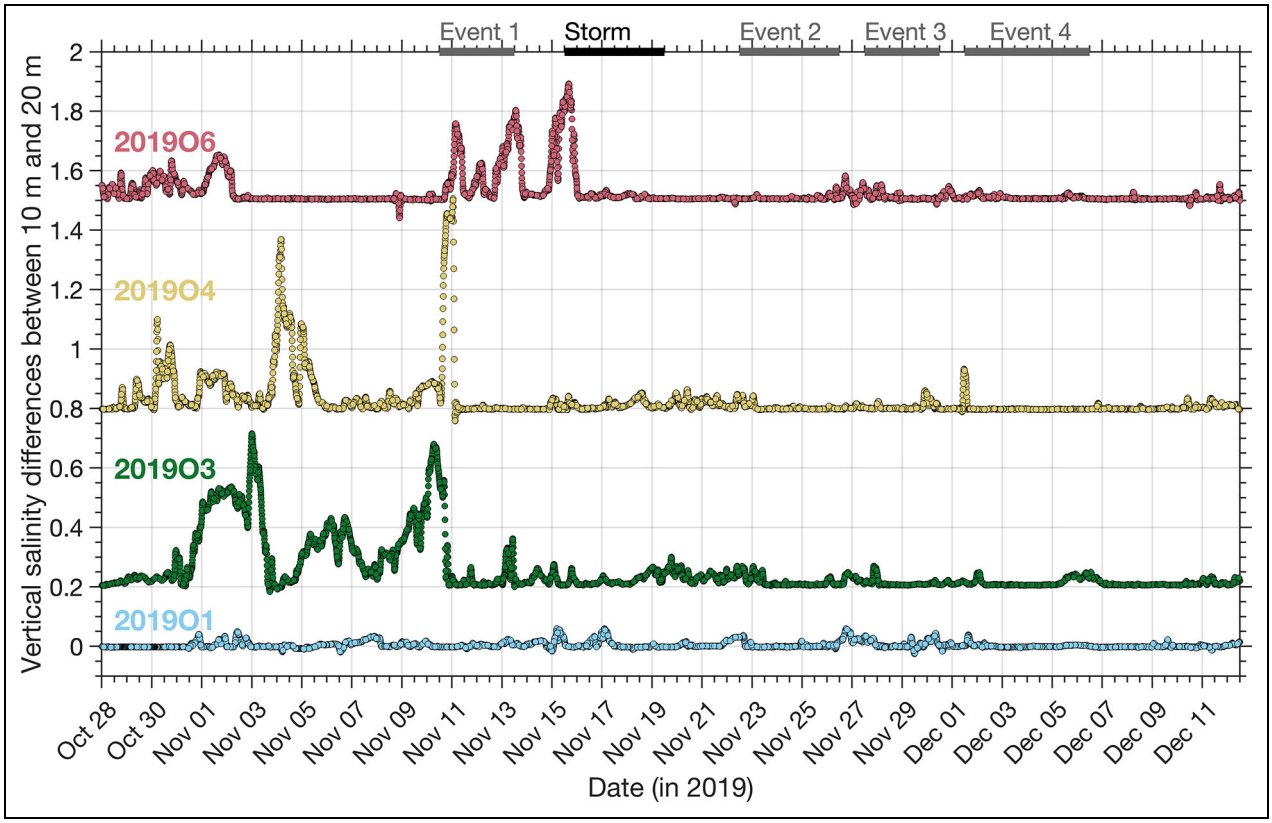

Figure 8. Time series of near-surface vertical salinity differences. Salinity differences between the two uppermost CTDs (nominal depths: 10 m and 20 m) on four Salinity-Ice-Tethered (SIT) buoys (color-coded): 2019O1, 2019O3, 2019O4, and 2019O6. Data have been scaled up vertically by adding 0.2 for 2019O3, 0.8 for 2019O4, and 1.5 for 2019O6 to allow better visualization. The four selected strong wind events (gray bars) and the storm (black bar) are indicated.

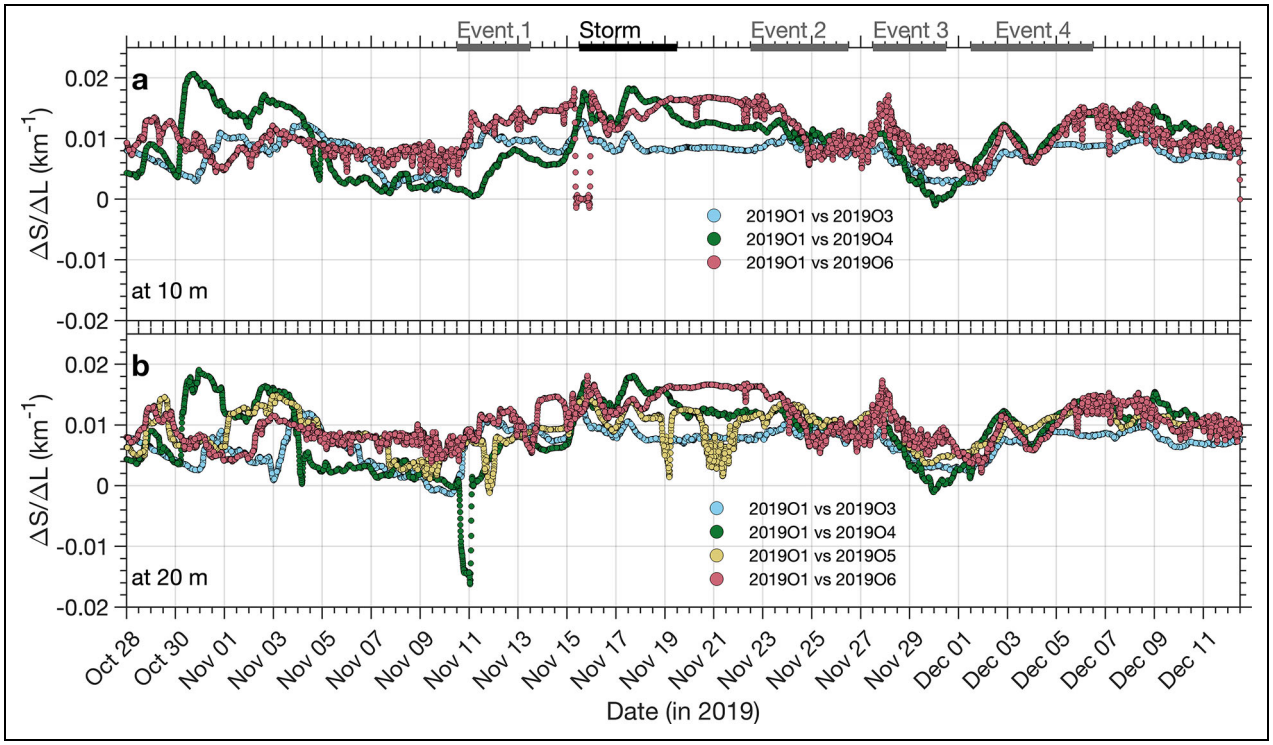

Figure 9. Time series of near-surface horizontal salinity differences. Salinity differences per kilometer of separation between CTDs at (a) 10 m and (b) 20 m depths of chosen Salinity-Ice-Tethered (SIT) buoy pairs (color-coded; see legend). The four selected strong wind events (gray bars) and the storm (black bar) are indicated.

intrahalocline eddy. Considering they were separated from each other by 25–60 km in a line approximately 60 km long suggests that the observed large salinity difference during the November 10–12 period was the manifestation of an eddy.

Except for the relatively large salinity differences indicative of the passage of an eddy, a typical value for a salinity difference in **Figure 8** was about 0.1–0.2, which is approximately equivalent to a $\Delta\sigma_\theta$ of 0.08–0.16 kg m^{-3}. **Figure 8** may thus be interpreted as a shallower analog of the blue line shown in **Figure 7**. Again, the pattern shown in **Figure 8** implies that the weakly stratified barrier layer was distributed patchily around the MOSAiC floes and its presence was not influenced by wind forcing.

The 10-minute resolution data from the SIT buoys can also be used to assess the state of near-surface horizontal stratification. We calculated salinity differences per kilometer separating buoys ($\Delta S/\Delta L$, where ΔS is the salinity difference and ΔL is the distance between buoys) at each time step from buoy pairs along 10 m and 20 m depths (**Figure 9**). The buoy separations for pairs 2019O1–2019O3 and 2019O1–2019O5 were about 60–70 km, and those for pairs 2019O1–2019O4 and 2019O1–2019O6 were about 30–40 km. Differentials among the curves may imply a salinity gradient within 15–20 km. The results shown in **Figure 9** indicate that different buoy pairs yielded varying horizontal salinity gradients during Leg 1, suggesting such horizontal salinity (or density) gradients were pervasive in the upper 20-m water column. If the upper 20-m ocean was spatially uniform or hosted only much larger-scale density gradients, observed horizontal salinity differences should be close to zero or similar with each other for most of the time. However, this expectation is not the general picture seen here with these horizontal salinity gradients still persisting despite the influence of storm and strong wind events.

Data from the buoy pair 2019O1–2019O4 even shows a V-shaped evolution of the horizontal salinity gradients at 20 m depth (green dots in **Figure 9b**) on November 10–11. Three other V-shaped patterns can be also found on November 12, 19, and 21 for the pair 2019O1–2019O5 (yellow dots in **Figure 9b**). We believe these V-shaped signatures reflect the two buoys encountering of intrahalocline eddies. Supportive evidence is presented in **Figure 10**. The buoy 2019O4 encountered an eddy on November 11, 2019, with strong westward flow of about 10 cm s^{-1} during the second half of the day (**Figure 10a**). The density evolution as determined from the buoy exhibited an upwelling at 20 m depth with denser water from below (σ_θ increasing 0.5 kg m^{-3}) and downwelling at 50 m depth with lighter water from above (σ_θ decreasing 0.2 kg m^{-3}) (**Figure 10b**). The combined effect was reduced stratification, indicating a convex-shaped anticyclonic eddy. This finding supports our previous interpretation of the large salinity differences seen on November 10–12 (**Figure 8**) in a sequence from buoys 2019O3, 2019O4, and 2019O6, indicating the eddy indeed propagated westward.

A similar eddy-like but less distinct density evolution was observed at buoy 2019O5 one day later on November 12 when a downwelling signature was detected at 100 m depth. The less pronounced signal in buoy 2019O5 data

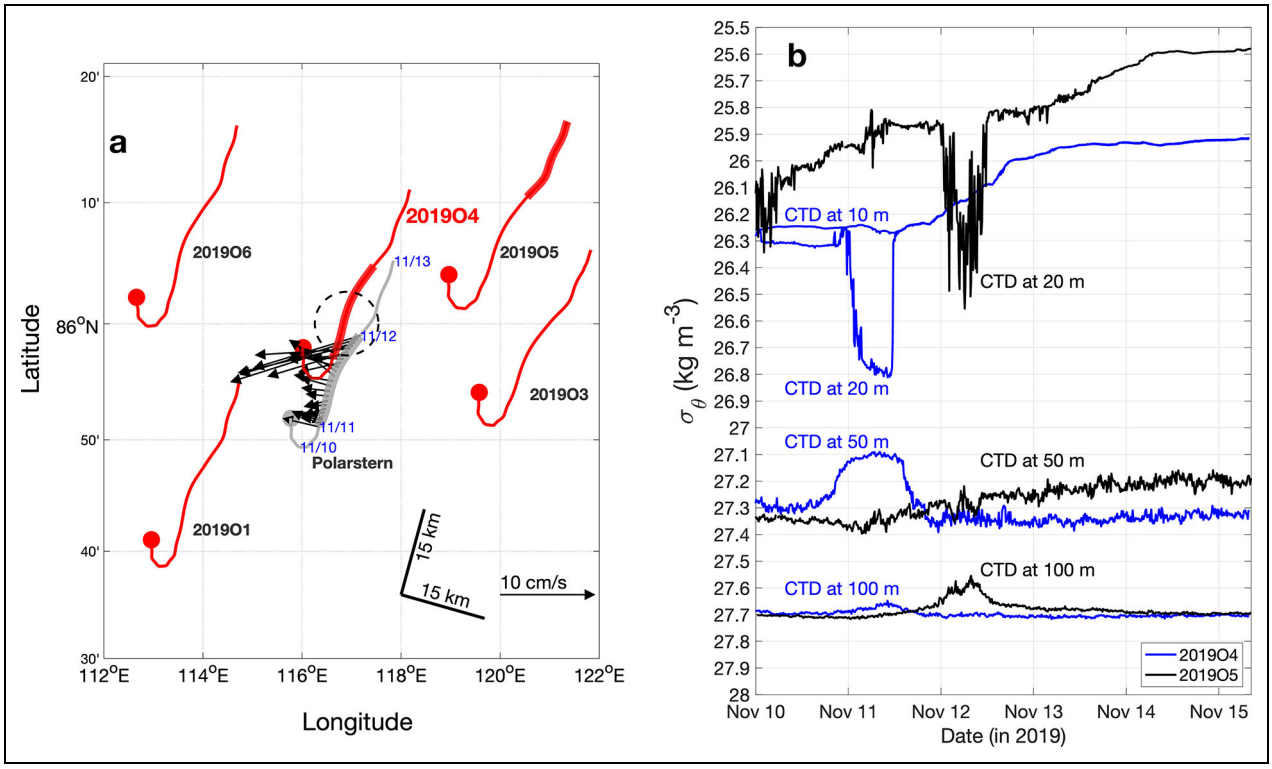

Figure 10. Intrahalocline eddy observed on the main ice floe and in the Distributed Network. (a) Track of R/V *Polarstern* (gray) and Salinity-Ice-Tethered (SIT) buoys (red). Red and gray dots indicate the starting positions of the trajectories. SADCP-derived depth-averaged currents for the upper 60 m are also included as black arrows to the ship path. Trajectories of SIT buoys 2019O4 and 2019O5 and of R/V *Polarstern* on November 11, 2019, are highlighted by thicker lines. The approximate location of the eddy is indicated by the dashed circle. (b) Density observations from SIT buoys 2019O4 (blue) and 2019O5 (black). Note that the y-axis is reversed with the density increasing downward.

suggests that the buoy did not fully encounter the center of the eddy. In aggregate, the results presented in **Figures 7**–**10** underline the dynamical central Arctic upper ocean during early winter. Importantly, we interpret that internal ice stresses dampen momentum transfer from strong storms to the upper ocean, rendering wind forcing insufficient to erode preexisting stratification under full sea ice cover. This may explain why the observed vertical and horizontal thermohaline gradients persisted throughout our observations and is consistent with the atmosphere-ice-ocean momentum transfer reported by Rabe et al. (2024; their figures 10 and 14) for parts of the winter period during the MOSAiC drift.

An interesting exercise is to examine the impact of the storm by computing horizontal wavenumber spectra of potential density with data from the two pre-storm and post-storm tracks (see **Figure 1a**). **Figure 11** shows that best-fit spectral slopes in the wavenumber range of 0.1–5 cpkm were close to −2.6 at surface mixed layer depths (10 m and 20 m), and −1.3 in the Arctic cold halocline layer and upper pycnocline (50 m, 75 m, and 100 m) in both periods. A spectral slope close to −3 in horizontal wavenumber spectra is commonly observed in the Arctic surface mixed layer (Timmermans et al., 2012; Timmermans and Winsor, 2013; Mackinnon et al., 2016). Different slopes for the surface mixed layer and pycnocline layer have been observed in the subtropical North Pacific (Callies and Ferrari, 2013), as is the case of our Arctic observations shown in **Figure 11**. These differences indicate the existence of two dynamical regimes in the surface mixed layer and the stratified water column below. The spectral slopes relatively flatter than the canonical slope of −5/3 (Marcinko et al., 2015) in the halocline layer suggest that there is more energy at small scales, which may be related to internal waves. These interpretations are unaffected by the lack of change due to the passing storm. A thorough discussion of horizontal wavenumber spectra is beyond the scope of this article; a more detailed discussion can be found in Callies and Ferrari (2013) and Callies et al. (2015).

4.3. Ocean current observations during Leg 1

We have seen that the water column in the 30–200 m depth range was highly stratified. Above depths of 30 m in the mixed layer, sea ice movement was largely coherent with wind forcing, resulting in prevailing near-inertial motion. Ideally, the SADCP of R/V *Polarstern* could have been used to resolve details of near-surface currents, if it had collected data above depths of 25 m. Fortunately, AOFB-installed ADCPs filled the data gap, allowing us to present the ocean currents observed in **Figures 12** and **13**. To facilitate interpretation, the time series of estimated MLDs using $\Delta\sigma_\theta$= 0.01 kg m^{-3} (see **Figure 7**) is superimposed on time series in both figures.

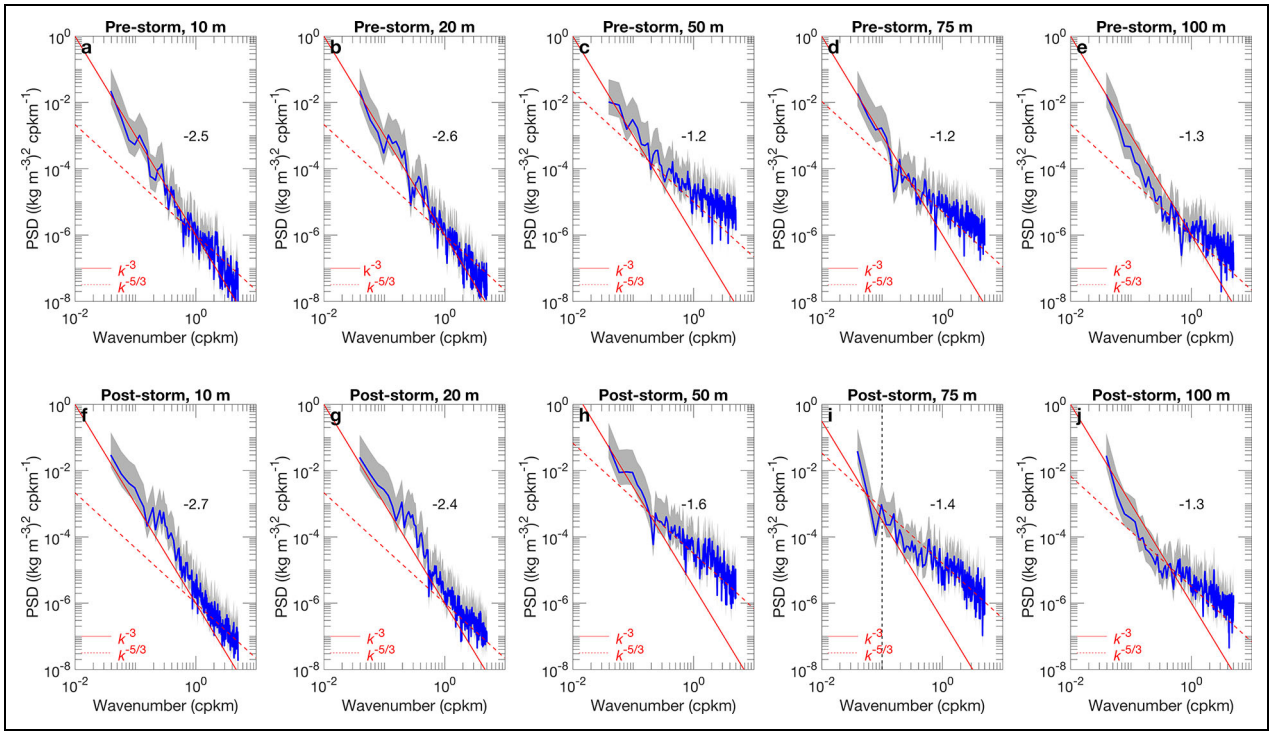

Figure 11. Along-track horizontal wavenumber spectra of potential density derived from SIT buoy 2019O1. (a–e) Horizontal wavenumber spectra of potential density (as power spectral density, PSD, in $(\text{kg m}^{-3})^2\ \text{cph}^{-1}$) derived from CTD readings at the five nominal depths of Salinity-Ice-Tethered (SIT) buoy 2019O1 along the pre-storm track. (f–j) Corresponding data along the post-storm track. Gray shading is the 95% confidence interval. Best-fit lines of slopes of −3 (red solid) and −5/3 (red dashed) are shown. Values of spectral slopes within the wavenumber range of 0.1–5 cpkm are provided in each figure. For example, the spectral slope in (a) is −2.5.

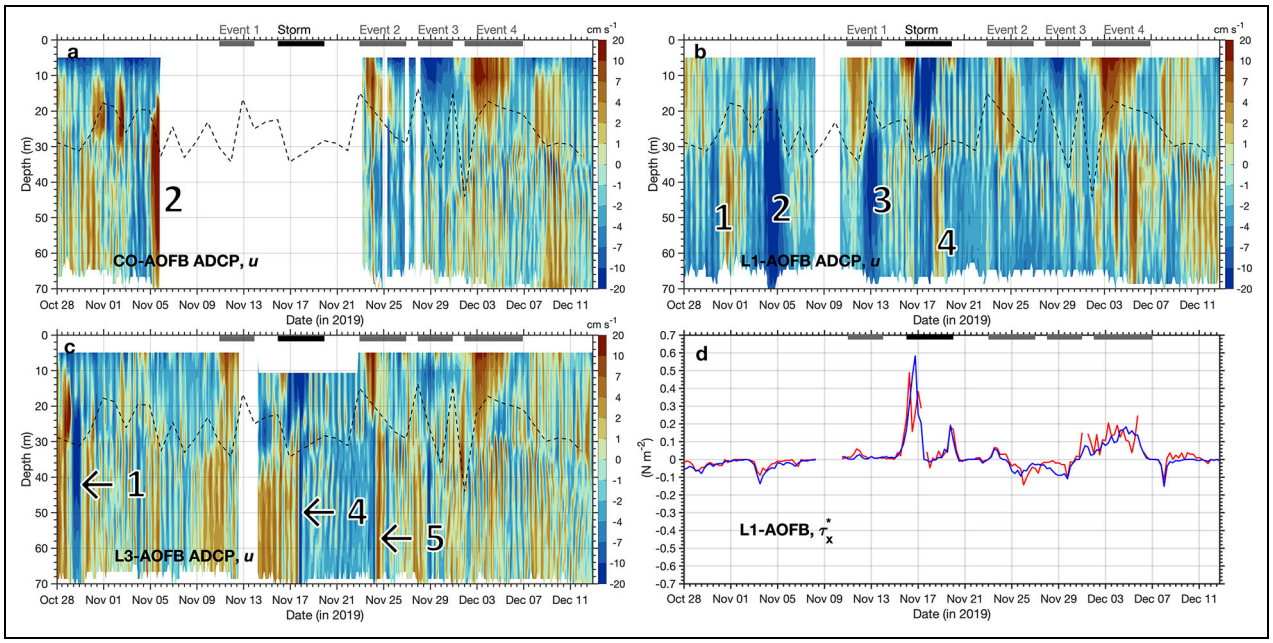

Figure 12. Time series of ocean current observations (zonal component) from AOFBs at CO, L1, and L3. Time series of the zonal (u, in cm s^{-1}) component of ADCP current measurements from Autonomous Ocean Flux Buoys (AOFBs) at (a) Central Observatory (CO), (b) site L1, and (c) site L3. (d) Estimated zonal frictional stress (τ_x^*) using Equation 4 (blue line) and Equations 5 and 6 (red line). The four selected strong wind events (gray bars) and the storm (black bar) are indicated. In (a–c), numbers 1–5 denote identified eddies and the dashed line is the estimated mixed layer depth.

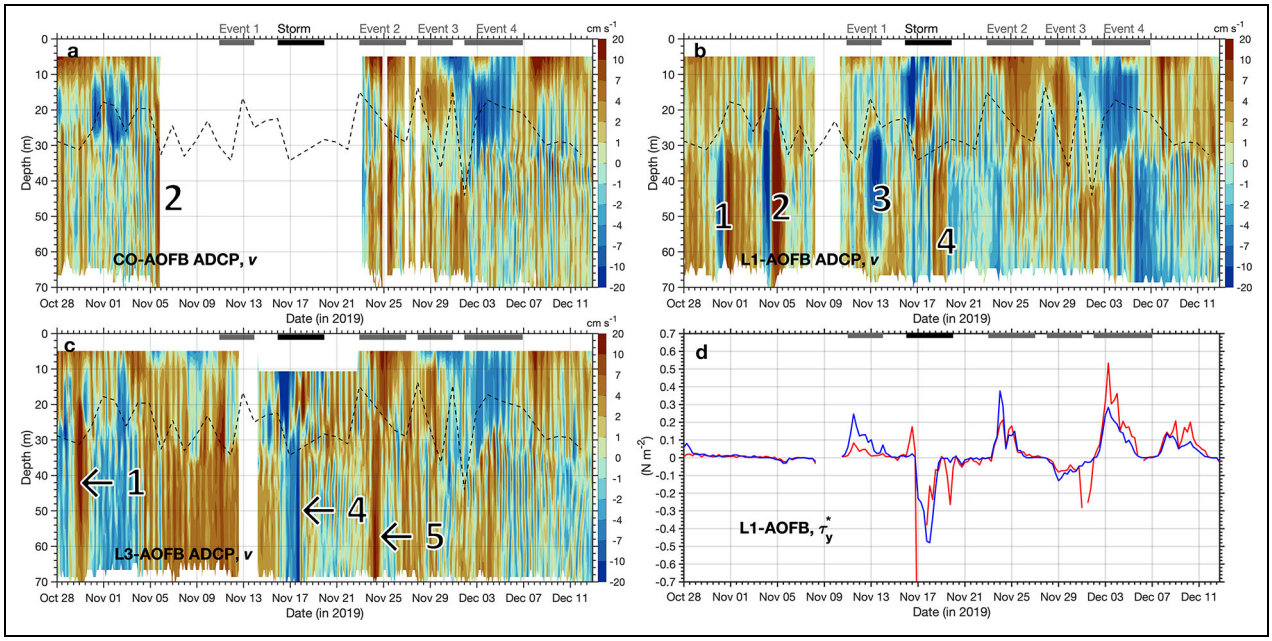

Figure 13. Time series of ocean current observations (meridional component) from AOFBs at CO, L1, and L3. Time series of the meridional (v, in cm s^{-1}) component of ADCP current measurements from Autonomous Ocean Flux Buoys (AOFBs) at (a) Central Observatory (CO), (b) site L1, and (c) site L3. (d) Estimated meridional frictional stress (τ_y^*) using Equation 4 (blue line) and Equations 5 and 6 (red line). The four selected strong wind events (gray bars) and the storm (black bar) are labeled. In (a–c), numbers of 1–5 denote identified eddies and the dashed line is the estimated mixed layer depth.

The observed flow fields generally contained three types of flow: (i) forced currents, (ii) eddies, and (iii) near-inertial currents. We explain the interpretation of these types as follows. Forced currents were mainly the result of accelerated sea ice motion due to impinging strong winds. These forced flows were confined within the mixed layer and lasted several days. Their appearance was aligned with the timing of the associated wind event. A clear example is the strong forced flow (>20 cm s^{-1}) above a depth of 10 m due to the November 16–19 storm, which L1 ADCP data show as an eastward-westward transition (**Figure 12b**). This transition is also consistent with the floe drift trajectory (see the yellow track in **Figure 1a**).

Following the approach of Carpenter and Timmermans (2012) to determining an eddy, we simply tracked the velocity data among the different ADCPs of the AOFBs. An eddy is determined either by anomalously large flow speed (>10 cm s^{-1}) compared to the general background flow (about 5 cm s^{-1}), or by a positive-negative alternating velocity pattern occurring within about 2 days. The former condition reflects that the eddy's core did not encounter the AOFB so a single velocity maximum is recorded. The latter indicates that the eddy's core passed through the footprint of the AOFB's ADCP so two velocity maxima are recorded. In total five eddies fulfilled these criteria, and we number them 1–5, placing them in **Figures 12** and **13** to identify their depths in the water column. The observed eddies were all in a similar depth range below the MLD and above a depth of 80 m and may be categorized as shallow intrahalocline eddies (Carpenter and Timmermans, 2012; Zhao and Timmermans, 2016). The case shown in **Figure 10b** recorded by the buoy 2019O4 is actually eddy number 3 shown in **Figures 12** and **13**.

Near-inertial currents, characterized by alternating positive-negative values, can be seen in **Figures 12** and **13** as banded stripes in their u or v components. These banded features were mostly oriented vertically and appeared twice a day in a patchy manner in the mixed layer (e.g., see **Figure 13b**, around November 20–21), an indication of forced near-inertial current. Some banded stripes below MLDs became slanted (e.g., see **Figures 12** and **13** from the start of December), implying signatures of NIWs (Halle and Pinkel, 2003; Pinkel, 2008). Note that fully separating near-inertial signals from semidiurnal currents around the critical latitude is not possible (Baumann et al., 2020).

Surprisingly, the two different frictional stress approaches produced results which are quantitatively similar to each other (**Figures 12d** and **13d**), though the ones produced by the flux package sensor on the AOFB (red line) had more data gaps and seem to have been noisier. That ice-water stress becomes the main contributor acting on the upper ocean is obvious. This finding corroborates our previous result of highly coupled wind-ice interaction (**Figure 3**), so that momentum from the atmosphere can be still transferred through full ice cover to the waters of the underlying ocean. Note that the frictional stresses substantially increased as the storm and other wind events began, but these increases weakened afterward. We believe that this pattern was a consequence of the ice-ocean stress governor (Meneghello et al., 2018), a mechanism or principle which states that ice-forced

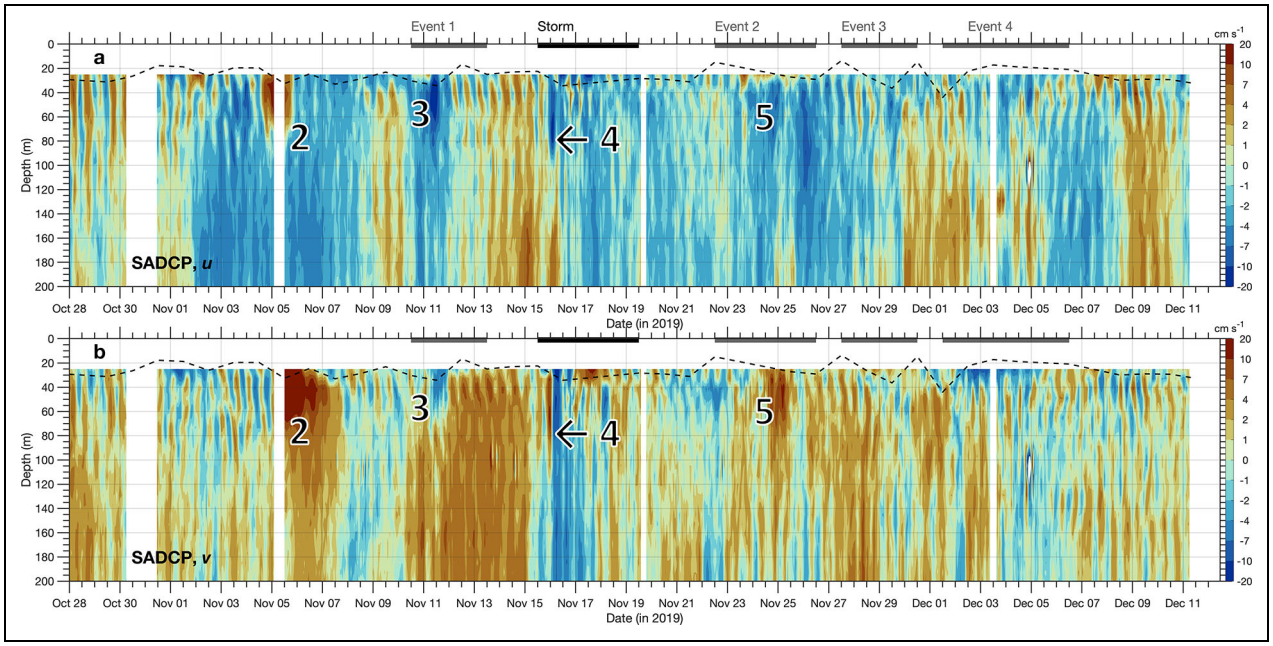

Figure 14. Time series of SADCP ocean current observations. Time series of R/V *Polarstern* SADCP measurements: (a) zonal and (b) meridional components (u and v, in cm s^{-1}, respectively). The four strong wind events (gray bars) and the storm (black bar) are indicated. In (a) and (b), the numbers 2–5 denote identified eddies. The dashed line is the estimated mixed layer depth.

current speeds eventually match ice drift speeds, shutting down surface stress. As it has fewer data gaps, we use the frictional stresses (blue lines in **Figures 12d** and **13d**) of Equation 4 for our slab model analysis.

The SADCP data of R/V *Polarstern* have a lower resolution (an 8-m bin size) but provide a wider range of ocean velocity readings down to a depth of 200 m (**Figure 14**). Four of the identified eddies situated above a depth of 100 m and below the MLDs shown in **Figures 12** and **13** can be seen in the SADCP data at these lower depths. The flow fields related to eddies are comparatively the strongest (>20 cm s^{-1}) among the SADCP observations. Patches of alternating positive-negative stripes at various vertical scales are also seen in the u or v components observed at depth. The vertical shear of the WKB-scaled and near-inertial-fitted (Section 3.5) zonal (du/dz) and meridional (dv/dz) velocities is shown in **Figure 15**. This presentation accounts for the stratification effect and removes signals of barotropic semidiurnal tides, revealing the presence of NIWs as alternating stripes populating the depths below the mixed layer. As sea ice coherently moves with the winds, **Figure 15** suggests that NIWs were persistently excited by it and were pervasive in the upper ocean during Leg 1. Previous studies have found that NIWs will become trapped inside an anticyclonic eddy and result in elevated turbulence near the bottom edge of the eddy (Kawaguchi et al., 2016). The observed intrahalocline eddies (see numbers 2–5 in **Figure 15**) also collocated at the depths where NIWs existed. A future topic relating intrahalocline eddies and NIWs in the central Arctic Ocean is one that deserves detailed investigation.

The signatures of stripes with upward phase (e.g., a lower-left to upper-right orientation) situated at depths below 100 m are also notable. These upward phase patterns imply the existence of NIWs with downward energy propagation (Halle and Pinkel, 2003; Fer, 2014). We computed vertical wavenumber spectra of the vertical shear shown in **Figure 15** following Alford et al. (2012) and separated the spectra in terms of upward and downward energy (not shown). We found the downward energy spectrum to be about two times larger for a vertical length scale of about 60 m, which is close to the observed upward phase pattern (note: the resolved Nyquist vertical wavelength was 16 m). Thus, we interpret this downward NIW propagation below depths of 100 m as very possibly to be radiated from the surface.

We notice that the storm in **Figure 15** was not associated with stronger NIW signals than the four strong wind events. Additionally, clear NIW signals were found before November 5, but at the time surface frictional stress was small (**Figures 12d** and **13d**). These discrepancies may be attributable to two factors. One is MOSAiC floe detection of NIWs generated from remote locations. The other is the wandering trajectory with varying drifting speeds of the MOSAiC floe, which could potentially have caused SADCP bias measuring NIW fields. However, whether these two possibilities were factors here is difficult to determine. Further study is needed in the future.

The impact of the storm on the upper ocean was evaluated with the mixed layer slab model (Section 3.7). Using the observed surface frictional stresses as forcing (**Figure 16a**), a comparison between the predicted near-inertial currents against the observed currents at 15 m depth from the ADCP of the L1 AOFB is presented in **Figure 16b** and **c**. The predicted near-inertial currents are reasonably reproduced and consistent with the observed

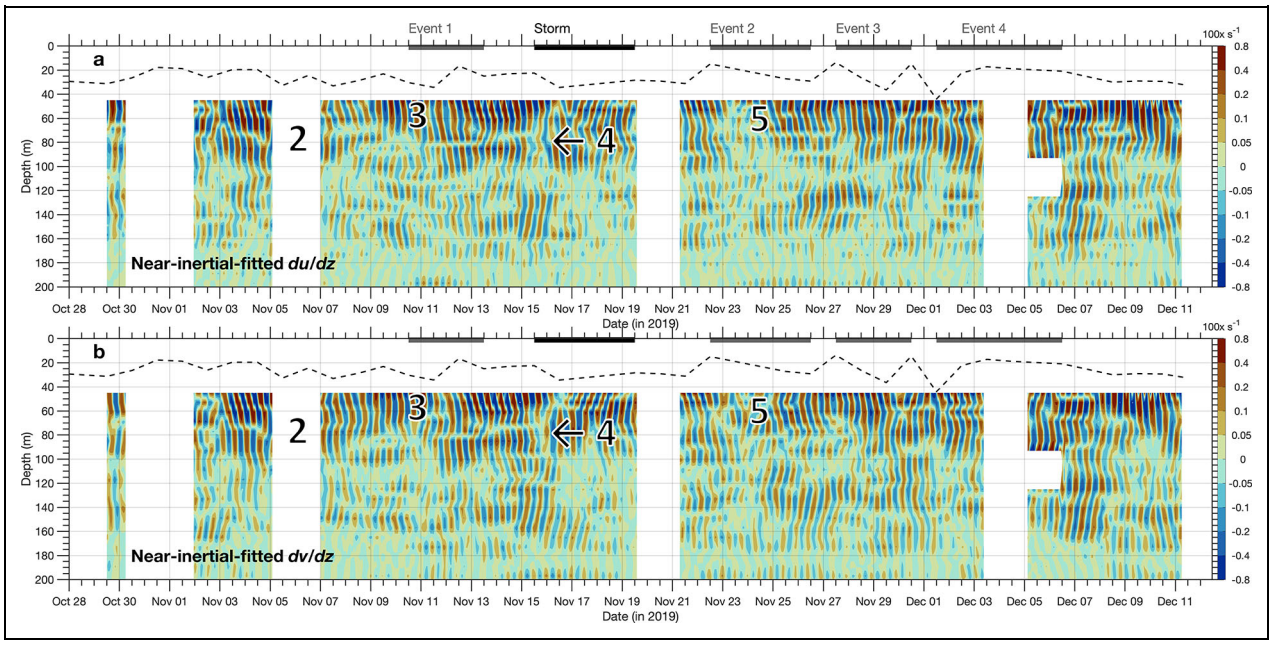

Figure 15. Time series of vertical shear of near-inertial-fitted ocean currents. Time series of hourly vertical shear of WKB-scaled and near-inertial-fitted horizontal velocities: (a) zonal and (b) meridional components (du/dz and dv/dz in s^{-1}, respectively), derived from the SADCP measurements of R/V *Polarstern*. The four strong wind events (gray bars) and the storm (black bar) are indicated. In (a) and (b), the numbers 2–5 denote the eddies identified in **Figure 14**. The dashed line is the estimated mixed layer depth.

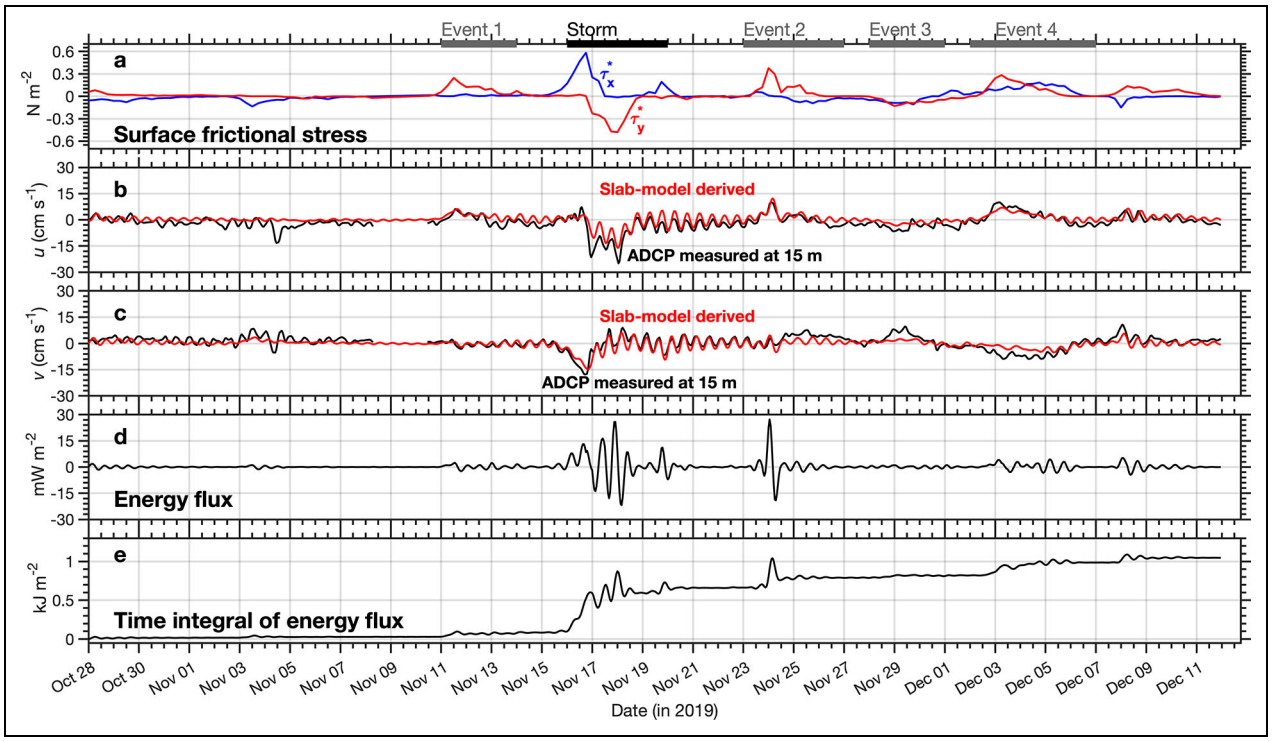

Figure 16. Time series of simulation of a mixed layer slab model. Time series of (a) observed hourly zonal (blue) and meridional (red) surface frictional stress from the Autonomous Ocean Flux Buoy (AOFB) at site L1; (b) zonal and (c) meridional currents predicted by the mixed layer slab model (red) and AOFB ADCP zonal and meridional currents (black) observed at a depth of 15 m, respectively; (d) predicted energy flux from the surface frictional stress to near-inertial currents in the mixed layer; and (e) the time integral of energy flux. The four strong wind events (gray bars) and the storm (black bar) are indicated.

currents, particularly during the storm. The slab model shows that the strong wind events 2 and 4 each contributed about 12% of the overall cumulative energy gain of 1.05 kJ m^{-2}, leading the other two strong wind events individually providing 4% of the overall energy. The storm clearly contributed much more energy flux into the mixed layer and accounted for 53% of the cumulative energy (**Figure 16d** and **e**). In aggregate, these wind events together provided 85% of the energy input in the mixed layer, underlining the role of the winter storm transfer of energy into the upper ocean.

5. Conclusions

We report a unique early winter 46-day-long series of observations obtained during the first leg of the MOSAiC expedition in the ice-covered central Arctic in 2019/2020. These observations were collected from a network of passively drifting ice floes on which crewed ice camps and autonomous buoys were established and deployed. The icebreaker R/V *Polarstern* was part of this drifting network and routinely supported ship-based observations. Four periods of strong wind in addition to a specific storm event were experienced in the drift, during which the surrounding seas were nearly 100% covered by sea ice. Moving coherently with the winds, this sea ice almost made up all surface forcing on the upper ocean. This environmental configuration allowed us to investigate the complex atmosphere-ice-ocean system, focusing on upper 200-m ocean variability, and in particular, on the oceanic response before and after the storm.

The MOSAiC floes encountered oceanic surface mixed layers with thicknesses varying from 15 m to 45 m. Some of these layers capped a weakly stratified barrier layer, a consequence of frontal dynamics. The mixed layers deepened during the beginning of wind events, possibly due to shear-driven mixing with greater ice drift speeds and increasing ice-water stress. High-resolution hydrographic observations at 10-minute sampling intervals from different ice floes revealed persistent vertical and horizontal density gradients in the upper 30 m, implying an upper central Arctic Ocean rich in surface frontal systems. These results corroborate observations of varying mixed layer depths and signatures of underlying barrier layers. The storm and other wind forcing seem to have had only a minor impact on the horizontal density gradients. Some of the observed density gradients were anomalously large and occurred on a time scale of 1–2 days. Our analyses provide evidence that these anomalous signals were related to intrahalocline eddies. Horizontal wavenumber spectra of density, showing a forward cascade of energy on large to small length scales, also were similar before and after the storm. Two distinct regimes in the top 100 m were characterized by the shapes of their spectra which separated the relatively mixed upper 20-m water column from the deeper heavily stratified layer below. We conclude that momentum transfer from wind to ocean is dampened by internal ice stresses in the absence of significant open water areas. This dampening means that although internal waves were generated by wind-driven ice movement, direct wind forcing was insufficient to erode the preexisting stratification under full sea ice cover. This conclusion explains why vertical and horizontal thermohaline gradients could persist throughout the period of our observations.

From our analysis of the observed ocean current data, we conclude the dynamics to be as follows. Flows within the surface mixed layer can be characterized as taking place by means of two mechanisms. First, amplified flows primarily derive from accelerating ice drift under strong winds. These forced flows can last several days until the winds and sea ice drift subside. The second type is surface forcing of near-inertial currents, which are excited by sea ice near-inertial drift responding strongly to the winds.

Underneath the mixed layer and in the range of the cold halocline layer, episodic intrahalocline eddies are responsible for the most dominant signal. They are generally revealed by one or two velocity maxima that are about one order larger than the ambient flow field. Underneath the mixed layer, the increasingly stratified water column also allows for the existence of internal waves, consisting of near-inertial internal waves and semidiurnal tides. Periodic, two-times a day, alternating patterns can be seen in the velocity data. After applying a scaling method to account for the stratification effect on internal waves and removing the barotropic tides, we found that near-inertial internal waves were most apparent underneath the base of the mixed layer and were prevalent at depths shallower than 100 m during the drift. The appearance of these near-inertial internal waves partially coincided with strong wind periods. Some near-inertial internal waves were also found deeper than 100 m with a signature of downward energy propagation. Our slab model analysis predicted the storm had the potential to provide half the overall near-inertial energy input into the mixed layer. In aggregate, these findings suggest that several processes strongly link surface variability to internal waves in the upper Arctic Ocean during winter.

Our article underlines the complexity of the coupled atmosphere-ice-ocean system. Full sea ice cover largely isolates the upper ocean from direct influence of the atmosphere, but the sea ice itself acts as a channel for atmosphere-ocean contact by responding coherently to atmospheric events and thus becomes the main driving force on the upper ocean. Without the complex network of deployed sensors and instruments, studying this atmosphere-ice-ocean system coupling during the Arctic winter would have been very difficult. We hope that our results can help to improve state-of-the-art models of Arctic climate prediction. More scientific questions are likely to be answered by investigating the comprehensive MOSAiC data sets in the future.

Data accessibility statement

Data sources that were analyzed in this study can be accessed with the information below.

PS-CTD and OC-CTD data: https://doi.pangaea.de/10.1594/PANGAEA.959963 and https://doi.pangaea.de/10.1594/PANGAEA.959964. ITP data at L1 of MOSAiC DN: https://doi.org/10.7289/v5mw2f7x. SIT buoys data of MOSAiC DN: https://doi.pangaea.de/10.1594/PANGAEA.

940320. Meteorological data onboard R/V *Polarstern*: https://doi.pangaea.de/10.1594/PANGAEA.935221. Meteorological data at Met City of MOSAiC CO: https://arcticdata.io/catalog/view/doi%3A10.18739%2FA2PV6B83F. SADCP data of R/V *Polarstern*: https://doi.pangaea.de/10.1594/PANGAEA.916092. AOFB data of MOSAiC CO: https://arcticdata.io/catalog/view/doi%3A10.18739%2FA2SQ8QK2V. AOFB data at L1 of MOSAiC DN: https://arcticdata.io/catalog/view/doi%3A10.18739%2FA2610VT5W. AOFB data at L3 of MOSAiC DN: https://arcticdata.io/catalog/view/doi%3A10.18739%2FA26W96B3T. Sea ice concentration data: https://data.seaice.uni-bremen.de/modis_amsr2/geotiff/Arctic/. Additional references to data sets that are already publicly available are given in the text.

Acknowledgments

This work was carried out and data used in this manuscript were produced as part of the international Multidisciplinary drifting Observatory for the Study of the Arctic Climate (MOSAiC) with the tag MOSAiC20192020 (AWI_PS122_00). We thank all those who contributed to MOSAiC and made this endeavor possible (Nixdorf et al., 2021). We very much thank the crews of the research vessels *Akademik Fedorov* and *Polarstern* and the Russian icebreaker *Kapitan Dranitsyn*. We also thank the leadership and support of the cruise leaders in Leg 1, Thomas Krumpen, Vladimir Sokolov, Matthew Shupe, Marcel Nicolaus, and Markus Rex. We appreciate Dai-Jyun Yu's help in refining the figures in this paper.

Funding

The following projects and funding agencies contributed to this work:

- The Alfred-Wegener-Institut Helmholtz-Zentrum für Polar- und Meeresforschung (AWI) through its projects: AWI_OCEAN.
- Chinese Polar Environmental Comprehensive Investigation and Assessment Programs, funded by the Chinese Arctic and Antarctic Administration; Marine Science and Technology Fund of Shandong Province for Qingdao National Laboratory for Marine Science and Technology (Grant: 2018SDKJ0104-1) and Chinese Natural Science Foundation (Grant: 41941012).
- The Helmholtz Society strategic investment infrastructures FRAM (Frontiers in Arctic marine Monitoring) and MIDO (Multidisciplinary Ice-based Drifting Observatory).
- Starting fund for YF from National Sun Yat-sen University.
- The project EPICA in the research theme MARE:N - Polarforschung/MOSAiC funded by the German Federal Ministry for Education and Research with funding number 03F0889A.
- The European Commission for EU H2020 grant no. 101003472 (project Arctic PASSION).
- Parts of this work were funded by the German Federal Ministry for Education and Research (BMBF) and the Federal Ministry of Research, Technology and Space (BMFTR) through a German Academic Exchange Service (DAAD) project (Internal waves, frontal processes, vertical fluxes of heat/salt in Arctic Ocean; grant no. 7748842).
- Travel funding for YF to visit the Alfred-Wegener-Institut Helmholtz-Zentrum für Polar- und Meeresforschung (AWI) was provided by the National Science and Technology Council of Taiwan (project ID 114-2927-I-110-502).

Competing interests

All authors declare that they have no competing interests.

Author contributions

Contributed to conception and design: YF, BR, IK, MH, ST, JR.
Contributed to acquisition of data: All authors.
Contributed to analysis and interpretation of data: YF, BR, IK, MH, ST, JR.
Drafted and/or revised the article: All authors.
Approved the submitted version for publication: All authors.

References

Alexeev, VA, **Esau, I**, **Polyakov, IV**, **Byam, SJ**, **Sorokina, S.** 2012. Vertical structure of recent arctic warming from observed data and reanalysis products. *Climatic Change* **111**(2): 215–239. DOI: https://doi.org/10.1007/s10584-011-0192-8.

Alford, MH. 2001. Internal swell generation: The spatial distribution of energy flux from the wind to mixed layer near-inertial motions. *Journal of Physical Oceanography* **31**(8): 2359–2368. DOI: https://doi.org/10.1175/1520-0485(2001)031<2359:ISGTSD>2.0.CO;2.

Alford, MH, **Cronin, MF**, **Klymak, JM.** 2012. Annual cycle and depth penetration of wind-generated near-inertial internal waves at Ocean Station Papa in the Northeast Pacific. *Journal of Physical Oceanography* **42**(6): 889–909. DOI: https://doi.org/10.1175/JPO-D-11-092.1.

Baumann, TM, **Polyakov, IV**, **Padman, L**, **Danielson, S**, **Fer, I**, **Janout, M**, **Williams, W**, **Pnyushkov, AV.** 2020. Arctic tidal current atlas. *Scientific Data* **7**(1): 1–11. DOI: https://doi.org/10.1038/s41597-020-00578-z.

Callies, J, **Ferrari, R.** 2013. Interpreting energy and tracer spectra of upper-ocean turbulence in the submesoscale range (1–200 km). *Journal of Physical Oceanography* **43**(11): 2456–2474. DOI: https://doi.org/10.1175/JPO-D-13-063.1.

Callies, J, **Ferrari, R**, **Klymak, JM**, **Gula, J.** 2015. Seasonality in submesoscale turbulence. *Nature Communications* **6**: 6862. DOI: https://doi.org/10.1038/ncomms7862.

Carpenter, JR, **Timmermans, M-L.** 2012. Deep mesoscale eddies in the Canada Basin, Arctic Ocean. *Geophysical Research Letters* **39**(20). DOI: https://doi.org/10.1029/2012GL053025.

Cox, C, **Gallagher, M**, **Shupe, M**, **Persson, O**, **Blomquist, B**, **Grachev, A**, **Riihimaki, L**, **Kutchenreiter, M**, **Morris, V**, **Solomon, A**, **Brooks, I**, **Costa, D**,

Gottas, D, **Hutchings, J**, **Osborn, J**, **Morris, S**, **Preusser, A**, **Uttal, T.** 2023. Met city meteorological and surface flux measurements (Level 3 Final), Multidisciplinary Drifting Observatory for the Study of Arctic Climate (MOSAiC), central Arctic, October 2019–September 2020. Arctic Data Center. DOI: https://doi.org/10.18739/A2PV6B83F.

D'Asaro, EA. 1985. The energy flux from the wind to near-inertial motions in the surface mixed layer. *Journal of Physical Oceanography* **15**(8): 1043–1059. DOI: https://doi.org/10.1175/1520-0485(1985)015<1043:TEFFTW>2.0.CO;2.

Dugan, JP, **Morris, WD**, **Okawa, BS.** 1986. Horizontal wave number distribution of potential energy in the ocean. *Journal of Geophysical Research: Oceans* **91**(C11): 12993–13000. DOI: https://doi.org/10.1029/JC091iC11p12993.

Emery, WJ, **Thomson, RE.** 1997. *Data analysis methods in Physical Oceanography.* Oxford, UK: Pergamon.

Felden, J, **Möller, L**, **Schindler, U**, **Huber, R**, **Schumacher, S**, **Koppe, R**, **Diepenbroek, M**, **Glöckner, FO.** 2023. PANGAEA—Data Publisher for Earth & Environmental Science. *Scientific Data* **10**(1): 347. DOI: https://doi.org/10.1038/s41597-023-02269-x.

Fer, I. 2014. Near-inertial mixing in the Central Arctic Ocean. *Journal of Physical Oceanography* **44**(8): 2031–2049. DOI: https://doi.org/10.1175/JPO-D-13-0133.1.

Fong, AA, **Hoppe, CJM**, **Aberle, N**, **Ashjian, CJ**, **Assmy, P**, **Bai, Y**, **Bakker, DCE**, **Balmonte, JP**, **Barry, KR**, **Bertilsson, S**, **Boulton, W**, **Bowman, J**, **Bozzato, D**, **Bratbak, G**, **Buck, M**, **Campbell, RG**, **Castellani, G**, **Chamberlain, EJ**, **Chen, J**, **Chierici, M**, **Cornils, A**, **Creamean, JM**, **Damm, E**, **Dethloff, K**, **Droste, ES**, **Ebenh, O**, **Eggers, SL**, **Enge, A**, **Flores, H**, **Fransson, A**, **Frickenhaus, S**, **Gardner, J**, **Gelfman, CE**, **Granskog, MA**, **Graeve, M**, **Havermans, C**, **Heuze, C**, **Hildebrandt, N**, **Hill, TCJ**, **Hoppema, M**, **Immerz, A**, **Jin, H**, **Koch, BP**, **Kong, X**, **Kraberg, A**, **Lan, M**, **Lange, BA**, **Larsen, A**, **Lebreton, B**, **Leu, E**, **Loose, B**, **Maslowski, W**, **Mavis, C**, **Metfies, K**, **Mock, T**, **Müller, O**, **Nicolaus, M**, **Niehoff, B**, **Nomura, D**, **Nöthig, E-M**, **Oggier, M**, **Oldenburg, E**, **Olsen, LM**, **Peeken, I**, **Perovich, DK**, **Popa, O**, **Rabe, B**, **Ren, J**, **Rex, M**, **Rinke, A**, **Rokitta, S**, **Rost, B**, **Sakinan, S**, **Salganik, E**, **Schaafsma, FL**, **Schäfer, H**, **Schmidt, K**, **Shoemaker, KM**, **Shupe, MD**, **Snoeijs-Leijonmalm, P**, **Stefels, J**, **Svenson, A**, **Tao, R**, **Torres-Valdés, S**, **Torstensson, A**, **Toseland, A**, **Ulfsbo, A**, **Van Leeuwe, MA**, **Vortkamp, M**, **Webb, AL**, **Zhuang, Y**, **Gradinger, RR.** 2024. Overview of the MOSAiC expedition: Ecosystem. *Elementa: Science of the Anthropocene* **12**(1): 135. DOI: https://doi.org/10.1525/elementa.2023.00135.

Gonella, J. 1972. A rotary-component method for analysing meteorological and oceanographic vector time series. *Deep Sea Research and Oceanographic Abstracts* **19**(12): 833–846. DOI: http://dx.doi.org/10.1016/0011-7471(72)90002-2.

Graham, RM, **Cohen, L**, **Petty, AA**, **Boisvert, LN**, **Rinke, A**, **Hudson, SR**, **Nicolaus, M**, **Granskog, MA.** 2017. Increasing frequency and duration of Arctic winter warming events. *Geophysical Research Letters* **44**(13): 6974–6983. DOI: https://doi.org/10.1002/2017GL073395.

Guthrie, JD, **Morison, JH**, **Fer, I.** 2013. Revisiting internal waves and mixing in the Arctic Ocean. *Journal of Geophysical Research: Oceans* **118**(8): 3966–3977. DOI: https://doi.org/10.1002/jgrc.20294.

Halle, C, **Pinkel, R.** 2003. Internal wave variability in the Beaufort Sea during the winter of 1993/1994. *Journal of Geophysical Research: Oceans* **108**(C7): 3210. DOI: https://doi.org/10.1029/2000JC000703.

Hibler, WD. 1979. A dynamic thermodynamic sea ice model. *Journal of Physical Oceanography* **9**(4): 815–846. DOI: https://doi.org/10.1175/1520-0485(1979)009<0815:ADTSIM>2.0.CO;2.

Hoppmann, M, **Kuznetsov, I**, **Fang, Y-C**, **Rabe, B.** 2022a. Mesoscale observations of temperature and salinity in the Arctic Transpolar Drift: A high-resolution dataset from the MOSAiC Distributed Network. *Earth System Science Data Discussions* **14**(11): 4901–4921. DOI: https://doi.org/10.5194/essd-2022-66.

Hoppmann, M, **Kuznetsov, I**, **Fang, Y-C**, **Rabe, B.** 2022b. Processed data of CTD buoys 2019O1 to 2019O8 as part of the MOSAiC Distributed Network. PANGAEA. DOI: https://doi.org/10.1594/PANGAEA.940320.

Jaiser, R, **Nakamura, T**, **Handorf, D**, **Dethloff, K**, **Ukita, J**, **Yamazaki, K.** 2016. Atmospheric winter response to Arctic sea ice changes in reanalysis data and model simulations. *Journal of Geophysical Research: Atmospheres* **121**(13): 7564–7577. DOI: https://doi.org/10.1002/2015JD024679.

Kawaguchi, Y, **Itoh, M**, **Fukamachi, Y**, **Moriya, E**, **Onodera, J**, **Kikuchi, T**, **Harada, N.** 2019. Year-round observations of sea-ice drift and near-inertial internal waves in the Northwind Abyssal Plain, Arctic Ocean. *Polar Science* **21**: 212–223. DOI: https://doi.org/10.1016/j.polar.2019.01.004.

Kawaguchi, Y, **Koenig, Z**, **Nomura, D**, **Hoppmann, M**, **Inoue, J**, **Fang, Y-C**, **Schulz, K**, **Gallagher, M**, **Katlein, C**, **Nicolaus, M**, **Rabe, B.** 2022. Turbulent mixing during late summer in the ice–ocean boundary layer in the central Arctic Ocean: Results from the MOSAiC expedition. *Journal of Geophysical Research: Oceans* **127**(8): e2021JC017975. DOI: https://doi.org/10.1029/2021JC017975.

Kawaguchi, Y, **Nishino, S**, **Inoue, J**, **Maeno, K**, **Takeda, H**, **Oshima, K.** 2016. Enhanced diapycnal mixing due to near-inertial internal waves propagating through an anticyclonic eddy in the ice-free Chukchi Plateau. *Journal of Physical Oceanography* **46**(8): 2457–2481. DOI: https://doi.org/10.1175/JPO-D-15-0150.1.

Knust, R. 2017. Polar research and supply vessel POLARSTERN operated by the Alfred-Wegener-Institute. *Journal of Large-Scale Research Facilities* **3**: 1–8. DOI: https://doi.org/10.17815/jlsrf-3-163.

Krishfield, R, **Toole, J**, **Proshutinsky, A**, **Timmermans, ML.** 2008. Automated ice-tethered profilers for seawater observations under pack ice in all seasons. *Journal of Atmospheric and Oceanic Technology* **25**(11): 2091–2105. DOI: https://doi.org/10.1175/2008JTECHO587.1.

Kuznetsov, I, **Rabe, B**, **Androsov, A**, **Fang, Y-C**, **Hoppmann, M**, **Quintanilla-Zurita, A**, **Harig, S**, **Tippenhauer, S**, **Schulz, K**, **Mohrholz, V**, **Fer, I**, **Fofonova, V**, **Janout, M.** 2024. Dynamical reconstruction of the upper-ocean state in the central Arctic during the winter period of the MOSAiC expedition. *Ocean Science* **20**(3): 759–777. DOI: https://doi.org/10.5194/egusphere-2023-1353.

Kwok, R, **Untersteiner, N.** 2011. The thinning of Arctic sea ice. *Physics Today* **64**: 36.

Leaman, KD, **Sanford, TB.** 1975. Vertical energy propagation of inertial waves: A vector spectral analysis of velocity profiles. *Journal of Geophysical Research: Oceans* **80**(15): 1975–1978. DOI: https://doi.org/10.1029/JC080i015p01975.

Ludwig, V, **Spreen, G**, **Haas, C**, **Istomina, L**, **Kauker, F**, **Murashkin, D.** 2019. The 2018 North Greenland polynya observed by a newly introduced merged optical and passive microwave sea-ice concentration dataset. *Cryosphere* **13**(7): 2051–2073. DOI: https://doi.org/10.5194/tc-13-2051-2019.

Ludwig, V, **Spreen, G**, **Pedersen, LT.** 2020. Evaluation of a new merged sea-ice concentration dataset at 1 km resolution from thermal infrared and passive microwave satellite data in the Arctic. *Remote Sensing* **12**(19): 3183. DOI: https://doi.org/10.3390/rs12193183.

MacKinnon, JA, **Nash, JD**, **Alford, MH**, **Lucas, AJ**, **Mickett, JB**, **Shroyer, EL**, **Waterhouse, AF**, **Tandon, A**, **Sengupta, D**, **Mahadevan, A**, **Ravichandran, M**, **Pinkel, R**, **Rudnick, DL**, **Whalen, CB**, **Alberty, MS**, **Lekha, JS**, **Fine, EC**, **Chaudhuri, D**, **Wagner, GL.** 2016. A tale of two spicy seas. *Oceanography* **29**(2): 50–61. DOI: https://doi.org/10.5670/oceanog.2016.38.

Manucharyan, GE, **Timmermans, M-L.** 2013. Generation and separation of mesoscale eddies from surface ocean fronts. *Journal of Physical Oceanography* **43**(12): 2545–2562. DOI: https://doi.org/10.1175/JPO-D-13-094.1.

Marcinko, CLJ, **Martin, AP**, **Allen, JT.** 2015. Characterizing horizontal variability and energy spectra in the Arctic Ocean halocline. *Journal of Geophysical Research: Oceans* **120**(1): 436–450. DOI: https://doi.org/10.1002/2014JC010381.

Martini, KI, **Simmons, HL**, **Stoudt, CA**, **Hutchings, JK.** 2014. Near-inertial internal waves and sea ice in the Beaufort Sea. *Journal of Physical Oceanography* **44**(8): 2212–2234. DOI: https://doi.org/10.1175/JPO-D-13-0160.1.

McPhee, M, ed. 2008. Turbulence basics, in *Air-ice-ocean interaction: Turbulent ocean boundary layer exchange processes*. New York, NY: Springer: 39–63. DOI: https://doi.org/10.1007/978-0-387-78335-2_3.

Meneghello, G, **Marshall, J**, **Campin, J-M**, **Doddridge, E**, **Timmermans, M-L.** 2018. The ice-ocean governor: Ice-ocean stress feedback limits Beaufort Gyre spin-up. *Geophysical Research Letters* **45**(20): 11293–11299. DOI: https://doi.org/10.1029/2018GL080171.

Morison, JH, **Long, CE**, **Levine, MD.** 1985. Internal wave dissipation under sea ice. *Journal of Geophysical Research: Oceans* **90**(C6): 11959–11966. DOI: https://doi.org/10.1029/JC090iC06p11959.

Nicolaus, M, **Perovich, DK**, **Spreen, G**, **Granskog, MA**, **von Albedyll, L**, **Angelopoulos, M**, **Anhaus, P**, **Arndt, S**, **Belter, HJ**, **Bessonov, V**, **Birnbaum, G**, **Brauchle, J**, **Calmer, R**, **Cardellach, E**, **Cheng, B**, **Clemens-Sewall, D**, **Dadic, R**, **Damm, E**, **de Boer, G**, **Demir, O**, **Dethloff, K**, **Divine, DV**, **Fong, AA**, **Fons, S**, **Frey, MM**, **Fuchs, N**, **Gabarró, C**, **Gerland, S**, **Goessling, HF**, **Gradinger, R**, **Haapala, J**, **Haas, C**, **Hamilton, J**, **Hannula, H-R**, **Hendricks, S**, **Herber, A**, **Heuzé, C**, **Hoppmann, M**, **Høyland, KV**, **Huntemann, M**, **Hutchings, JK**, **Hwang, B**, **Itkin, P**, **Jacobi, H-W**, **Jaggi, M**, **Jutila, A**, **Kaleschke, L**, **Katlein, C**, **Kolabutin, N**, **Krampe, D**, **Kristensen, SS**, **Krumpen, T**, **Kurtz, N**, **Lampert, A**, **Lange, BA**, **Lei, R**, **Light, B**, **Linhardt, F**, **Liston, GE**, **Loose, B**, **Macfarlane, AR**, **Mahmud, M**, **Matero, IO**, **Maus, S**, **Morgenstern, A**, **Naderpour, R**, **Nandan, V**, **Niubom, A**, **Oggier, M**, **Oppelt, N**, **Pätzold, F**, **Perron, C**, **Petrovsky, T**, **Pirazzini, R**, **Polashenski, C**, **Rabe, B**, **Raphael, IA**, **Regnery, J**, **Rex, M**, **Ricker, R**, **Riemann-Campe, K**, **Rinke, A**, **Rohde, J**, **Salganik, E**, **Scharien, RK**, **Schiller, M**, **Schneebeli, M**, **Semmling, M**, **Shimanchuk, E**, **Shupe, MD**, **Smith, MM**, **Smolyanitsky, V**, **Sokolov, V**, **Stanton, T**, **Stroeve, J**, **Thielke, L**, **Timofeeva, A**, **Tonboe, RT**, **Tavri, A**, **Tsamados, M**, **Wagner, DN**, **Watkins, D**, **Webster, M**, **Wendisch, M.** 2022. Overview of the MOSAiC expedition: Snow and sea ice. *Elementa: Science of the Anthropocene* **10**(1). DOI: https://doi.org/10.1525/elementa.2021.000046.

Nixdorf, U, **Dethloff, K**, **Rex, M**, **Shupe, M**, **Sommerfeld, A**, **Perovich, DK.**, **Nicolaus, M**, **Heuzé, C**, **Rabe, B**, **Loose, B**, **Damm, E**, **Gradinger, R**, **Fong, A**, **Maslowski, W**, **Rinke, A**, **Kwok, R**, **Spreen, G**, **Wendisch, M**, **Herber, A**, **Hirsekorn, M**, **Mohaupt, V**, **Frickenhaus, S**, **Immerz, A**, **Weiss-Tuider, K**, **König, B**, **Mengedoht, D**, **Regnery, J**, **Gerchow, P**, **Ransby, D**, **Krumpen, T**, **Morgenstern, A**, **Haas, C**, **Kanzow, T**, **Rack, FR**, **Saitzev, A**, **Sokolov, V**, **Makarov, A**, **Schwarze, S**, **Wunderlich, T**, **Wurr, K**, **Boetius, A.** 2021. MOSAiC extended acknowledgement. *Zenodo*: 1–10. DOI: http://dx.doi.org/10.5281/%0Dzenodo.5541624.

Nurser, AJG, **Bacon, S.** 2014. The Rossby radius in the Arctic Ocean. *Ocean Science* **10**(6): 967–975. DOI: https://doi.org/10.5194/os-10-967-2014.

Pinkel, R. 2005. Near-inertial wave propagation in the western Arctic. *Journal of Physical Oceanography* **35**(5): 645–665. DOI: https://doi.org/10.1175/JPO2715.1.

Pinkel, R. 2008. The wavenumber–frequency spectrum of vortical and internal-wave shear in the western Arctic Ocean. *Journal of Physical Oceanography* **38**(2): 277–290. DOI: https://doi.org/10.1175/2006JPO3558.1.

Pollard, RT, **Millard, RC.** 1970. Comparison between observed and simulated wind-generated inertial oscillations. *Deep Sea Research and Oceanographic Abstracts* **17**(4): 813–821. DOI: https://doi.org/10.1016/0011-7471(70)90043-4.

Polyakov, IV, **Pnyushkov, AV**, **Alkire, MB**, **Ashik, IM**, **Baumann, TM**, **Carmack, EC**, **Goszczko, I**, **Guthrie, J**, **Ivanov, VV**, **Kanzow, T**, **Krishfield, R**, **Kwok, R**, **Sundfjord, A**, **Morison, J**, **Rember, R**, **Yulin, A.** 2017. Greater role for Atlantic inflows on sea-ice loss in the Eurasian Basin of the Arctic Ocean. *Science* **356**(6335): 285–291. DOI: https://doi.org/10.1126/science.aai8204.

Polyakov, IV, **Pnyushkov, AV**, **Charette, M**, **Cho, K-H**, **Jung, J**, **Kipp, L**, **Muilwijk, M**, **Whitmore, L**, **Yang, EJ**, **Yoo, J.** 2025. Atlantification advances into the Amerasian Basin of the Arctic Ocean. *Science Advances* **11**(8): eadq7580. DOI: https://doi.org/10.1126/sciadv.adq7580.

Polyakov, IV, **Pnyushkov, AV**, **Rember, R**, **Padman, L**, **Carmack, EC**, **Jackson, JM.** 2013. Winter convection transports Atlantic water heat to the surface layer in the eastern Arctic Ocean. *Journal of Physical Oceanography* **43**(10): 2142–2155. DOI: https://doi.org/10.1175/JPO-D-12-0169.1.

Quintanilla-Zurita, A, **Rabe, B**, **Wekerle, C**, **Kanzow, T**, **Kuznetsov, I**, **Torres-Valdes, S**, **Pallàs-Sanz, E**, **Fang, Y-C.** 2026. Intrahalocline eddies in the Amundsen Basin observed in the distributed network from the MOSAiC expedition. *Ocean Science* **22**: 305–328. DOI: https://doi.org/10.5194/os-22-305-2026.

Rabe, B, **Cox, CJ**, **Fang, Y-C**, **Goessling, H**, **Granskog, MA**, **Hoppmann, M**, **Hutchings, JK**, **Krumpen, T**, **Kuznetsov, I**, **Lei, R**, **Li, T**, **Maslowski, W**, **Nicolaus, M**, **Perovich, D**, **Persson, O**, **Regnery, J**, **Rigor, I**, **Shupe, MD**, **Sokolov, V**, **Spreen, G**, **Stanton, T**, **Watkins, DM**, **Blockley, E**, **Jakob Buenger, H**, **Cole, S**, **Fong, A**, **Haapala, J**, **Heuzé, C**, **Hoppe, CJM**, **Janout, M**, **Jutila, A**, **Katlein, C**, **Krishfield, R**, **Lin, L**, **Ludwig, V**, **Morgenstern, A**, **O'Brien, J**, **Zurita, AQ**, **Rackow, T**, **Riemann-Campe, K**, **Rohde, J**, **Shaw, W**, **Smolyanitsky, V**, **Solomon, A**, **Sperling, A**, **Tao, R**, **Toole, J**, **Tsamados, M**, **Zhu, J**, **Zuo, G.** 2024. The MOSAiC Distributed Network: Observing the coupled Arctic system with multidisciplinary, coordinated platforms. *Elementa: Science of the Anthropocene* **12**(1): 00103. DOI: https://doi.org/10.1525/elementa.2023.00103.

Rabe, B, **Heuzé, C**, **Regnery, J**, **Aksenov, Y**, **Allerholt, J**, **Athanase, M**, **Bai, Y**, **Basque, C**, **Bauch, D**, **Baumann, TM**, **Chen, D**, **Cole, ST**, **Craw, L**, **Davies, A**, **Damm, E**, **Dethloff, K**, **Divine, DV**, **Doglioni, F**, **Ebert, F**, **Fang, Y-C**, **Fer, I**, **Fong, AA**, **Gradinger, R**, **Granskog, MA**, **Graupner, R**, **Haas, C**, **He, H**, **He, Y**, **Hoppmann, M**, **Janout, M**, **Kadko, D**, **Kanzow, T**, **Karam, S**, **Kawaguchi, Y**, **Koenig, Z**, **Kong, B**, **Krishfield, RA**, **Krumpen, T**, **Kuhlmey, D**, **Kuznetsov, I**, **Lan, M**, **Laukert, G**, **Lei, R**, **Li, T**, **TorresValdés, S**, **Lin, L**, **Lin, L**, **Liu, H**, **Liu, N**, **Loose, B**, **Ma, X**, **MacKay, R**, **Mallet, M**, **Mallett, RDC**, **Maslowski, W**, **Mertens, C**, **Mohrholz, V**, **Muilwijk, M**, **Nicolaus, M**, **O'Brien, JK**, **Perovich, D**, **Ren, J**, **Rex, M**, **Ribeiro, N**, **Rinke, A**, **Schaffer, J**, **Schuffenhauer, I**, **Schulz, K**, **Shupe, MD**, **Shaw, W**, **Sokolov, V**, **Sommerfeld, A**, **Spreen, G**, **Stanton, T**, **Stephens, M**, **Su, J**, **Sukhikh, N**, **Sundfjord, A**, **Thomisch, K**, **Tippenhauer, S**, **Toole, JM**, **Vredenborg, M**, **Walter, M**, **Wang, H**, **Wang, L**, **Wang, Y**, **Wendisch, M**, **Zhao, J**, **Zhou, M**, **Zhu, J.** 2022. Overview of the MOSAiC expedition: Physical oceanography. *Elementa: Science of the Anthropocene* **10**(1): 00062. DOI: https://doi.org/10.1525/elementa.2021.00062.

Rainville, L, **Woodgate, RA.** 2009. Observations of internal wave generation in the seasonally ice-free Arctic. *Geophysical Research Letters* **36**(23): L23604. DOI: https://doi.org/10.1029/2009GL041291.

Rantanen, M, **Karpechko, AY**, **Lipponen, A**, **Nordling, K**, **Hyvärinen, O**, **Ruosteenoja, K**, **Vihma, T**, **Laaksonen, A.** 2022. The Arctic has warmed nearly four times faster than the globe since 1979. *Communications Earth & Environment* **3**(1): 168. DOI: https://doi.org/10.1038/s43247-022-00498-3.

Rinke, A, **Maturilli, M**, **Graham, RM**, **Matthes, H**, **Handorf, D**, **Cohen, L**, **Hudson, SR**, **Moore, JC.** 2017. Extreme cyclone events in the Arctic: Wintertime variability and trends. *Environmental Research Letters* **12**(9). DOI: https://doi.org/10.1088/1748-9326/aa7def.

Rudels, B, **Korhonen, M**, **Schauer, U**, **Pisarev, S**, **Rabe, B**, **Wisotzki, A.** 2015. Circulation and transformation of Atlantic water in the Eurasian Basin and the contribution of the Fram Strait inflow branch to the Arctic Ocean heat budget. *Progress in Oceanography* **132**: 128–152. DOI: https://doi.org/10.1016/j.pocean.2014.04.003.

Schmithüsen, H. 2021. Continuous meteorological surface measurement during POLARSTERN cruise PS122/1. PANGAEA. DOI: https://doi.org/10.1594/PANGAEA.935221.

Shaw, WJ, **Stanton, TP**, **McPhee, MG**, **Kikuchi, T.** 2008. Estimates of surface roughness length in heterogeneous under-ice boundary layers. *Journal of Geophysical Research: Oceans* **113**(8): 1–16. DOI: https://doi.org/10.1029/2007JC004550.

Shimada, K, **Kamoshida, T**, **Itoh, M**, **Nishino, S**, **Carmack, E**, **McLaughlin, F**, **Zimmermann, S**, **Proshutinsky, A.** 2006. Pacific Ocean inflow: Influence on catastrophic reduction of sea ice cover in the Arctic Ocean. *Geophysical Research Letters* **33**(8): L08605. DOI: https://doi.org/10.1029/2005GL025624.

Shupe, MD, **Rex, M**, **Blomquist, B**, **Persson, POG**, **Schmale, J**, **Uttal, T**, **Althausen, D**, **Angot, H**,

Archer, S, **Bariteau, L**, **Beck, I**, **Bilberry, J**, **Bucci, S**, **Buck, C**, **Boyer, M**, **Brasseur, Z**, **Brooks, IM**, **Calmer, R**, **Cassano, J**, **Castro, V**, **Chu, D**, **Costa, D**, **Cox, CJ**, **Creamean, J**, **Crewell, S**, **Dahlke, S**, **Damm, E**, **de Boer, G**, **Deckelmann, H**, **Dethloff, K**, **Dütsch, M**, **Ebell, K**, **Ehrlich, A**, **Ellis, J**, **Engelmann, R**, **Fong, AA**, **Frey, MM**, **Gallagher, MR**, **Ganzeveld, L**, **Gradinger, R**, **Graeser, J**, **Greenamyer, V**, **Griesche, H**, **Griffiths, S**, **Hamilton, J**, **Heinemann, G**, **Helmig, D**, **Herber, A**, **Heuzé, C**, **Hofer, J**, **Houchens, T**, **Howard, D**, **Inoue, J**, **Jacobi, H-W**, **Jaiser, R**, **Jokinen, T**, **Jourdan, O**, **Jozef, G**, **King, W**, **Kirchgaessner, A**, **Klingebiel, M**, **Krassovski, M**, **Krumpen, T**, **Lampert, A**, **Landing, W**, **Laurila, T**, **Lawrence, D**, **Lonardi, M**, **Loose, B**, **Lüpkes, C**, **Maahn, M**, **Macke, A**, **Maslowski, W**, **Marsay, C**, **Maturilli, M**, **Mech, M**, **Morris, S**, **Moser, M**, **Nicolaus, M**, **Ortega, P**, **Osborn, J**, **Pätzold, F**, **Perovich, DK**, **Petäjä, T**, **Pilz, C**, **Pirazzini, R**, **Posman, K**, **Powers, H**, **Pratt, KA**, **Preußer, A**, **Quéléver, L**, **Radenz, M**, **Rabe, B**, **Rinke, A**, **Sachs, T**, **Schulz, A**, **Siebert, H**, **Silva, T**, **Solomon, A**, **Sommerfeld, A**, **Spreen, G**, **Stephens, M**, **Stohl, A**, **Svensson, G**, **Uin, J**, **Viegas, J**, **Voigt, C**, **von der Gathen, P**, **Wehner, B**, **Welker, JM**, **Wendisch, M**, **Werner, M**, **Xie, ZQ**, **Yue, F.** 2022. Overview of the MOSAiC expedition: Atmosphere. *Elementa: Science of the Anthropocene* **10**(1). DOI: https://doi.org/10.1525/elementa.2021.00060.

Smith, KS. 2007. The geography of linear baroclinic instability in Earth's oceans. *Journal of Marine Research* **65**: 655–683. DOI: https://doi.org/10.1357/002224007783649484.

Stanton, TP, **Shaw, WJ.** 2023a. Observations from Autonomous Ocean Flux Buoy 46 deployed at site CO during the MOSAiC transpolar drift, Arctic Basin, 2019–2020. Arctic Data Center. DOI: https://doi.org/10.18739/A2SQ8QK2V.

Stanton, TP, **Shaw, WJ.** 2023b. Observations from Autonomous Ocean Flux Buoy 43 deployed at site L1 during the MOSAiC transpolar drift, Arctic Basin, 2019–2020. Arctic Data Center. DOI: https://doi.org/10.18739/A2610VT5W.

Stanton, TP, **Shaw, WJ.** 2023c. Observations from Autonomous Ocean Flux Buoy 45 deployed at site L3 during the MOSAiC transpolar drift, Arctic Basin, 2019–2020. Arctic Data Center. DOI: https://doi.org/10.18739/A26W96B3T.

Stroeve, JC, **Schroder, D**, **Tsamados, M**, **Feltham, D.** 2018. Warm winter, thin ice? *The Cryosphere* **12**(5): 1791–1809. DOI: https://doi.org/10.5194/tc-12-1791-2018.

Tang, Q, **Zhang, X**, **Yang, X**, **Francis, JA.** 2013. Cold winter extremes in northern continents linked to Arctic sea ice loss. *Environmental Research Letters* **8**(1). DOI: https://doi.org/10.1088/1748-9326/8/1/014036.

Timmermans, M-L, **Cole, S**, **Toole, J.** 2012. Horizontal density structure and restratification of the Arctic Ocean surface layer. *Journal of Physical Oceanography* **42**(4): 659–668. DOI: https://doi.org/10.1175/JPO-D-11-0125.1.

Timmermans, M-L, **Marshall, J.** 2020. Understanding Arctic Ocean circulation: A review of ocean dynamics in a changing climate. *Journal of Geophysical Research: Oceans* **125**(4): 1–35. DOI: https://doi.org/10.1029/2018JC014378.

Timmermans, M-L, **Toole, J**, **Proshutinsky, A**, **Krishfield, R**, **Plueddemann, A.** 2008. Eddies in the Canada Basin, Arctic Ocean, observed from ice-tethered profilers. *Journal of Physical Oceanography* **38**(1): 133–145. DOI: https://doi.org/10.1175/2007JPO3782.1.

Timmermans, M-L, **Winsor, P.** 2013. Scales of horizontal density structure in the Chukchi Sea surface layer. *Continental Shelf Research* **52**: 39–45. DOI: https://doi.org/10.1016/j.csr.2012.10.015.

Tippenhauer, S, **Rex, M.** 2020. Raw data of continuous VM-ADCP (vessel-mounted Acoustic Doppler Current Profiler) profile during POLARSTERN cruise PS122/1. PANGAEA. DOI: https://doi.org/10.1594/PANGAEA.916092.

Tippenhauer, S, **Vredenborg, M**, **Heuzé, C**, **Ulfsbo, A**, **Rabe, B**, **Granskog, MA**, **Allerholt, J**, **Balmonte, JP**, **Campbell, RG**, **Castellani, G**, **Chamberlain, E**, **Creamean, J**, **D'Angelo, A**, **Dietrich, U**, **Droste, ES**, **Eggers, L**, **Fang, YC**, **Fong, AA**, **Gardner, J**, **Graupner, R**, **Grosse, J**, **He, H**, **Hildebrandt, N**, **Hoppe, CJM**, **Hoppmann, M**, **Kanzow, T**, **Karam, S**, **Koenig, Z**, **Kong, B**, **Kuhlmey, D**, **Kuznetsov, I**, **Lan, M**, **Liu, H**, **Mallet, M**, **Mohrholz, V**, **Muilwijk, M**, **Müller, O**, **Olsen, LM**, **Rember, R**, **Ren, J**, **Sakinan, S**, **Schaffer, J**, **Schmidt, K**, **Schuffenhauer, I**, **Schulz, K**, **Shoemaker, K**, **Spahic, S**, **Sukhikh, N**, **Svenson, A**, **Torres-Valdés, S**, **Torstensson, A**, **Wischnewski, L**, **Zhuang, Y.** 2023a. Physical oceanography based on ship CTD during POLARSTERN cruise PS122. PANGAEA. DOI: https://doi.org/10.1594/PANGAEA.959963.

Tippenhauer, S, **Vredenborg, M**, **Heuzé, C**, **Ulfsbo, A**, **Rabe, B**, **Granskog, MA**, **Allerholt, J**, **Balmonte, JP**, **Campbell, RG**, **Castellani, G**, **Chamberlain, E**, **Creamean, J**, **D'Angelo, A**, **Dietrich, U**, **Droste, ES**, **Eggers, L**, **Fang, YC**, **Fong, AA**, **Gardner, J**, **Graupner, R**, **Grosse, J**, **He, H**, **Hildebrandt, N**, **Hoppe, CJM**, **Hoppmann, M**, **Kanzow, T**, **Karam, S**, **Koenig, Z**, **Kong, B**, **Kuhlmey, D**, **Kuznetsov, I**, **Lan, M**, **Liu, H**, **Mallet, M**, **Mohrholz, V**, **Muilwijk, M**, **Müller, O**, **Olsen, LM**, **Rember, R**, **Ren, J**, **Sakinan, S**, **Schaffer, J**, **Schmidt, K**, **Schuffenhauer, I**, **Schulz, K**, **Shoemaker, K**, **Spahic, S**, **Sukhikh, N**, **Svenson, A**, **Torres-Valdés, S**, **Torstensson, A**, **Wischnewski, L**, **Zhuang, Y.** 2023b. Physical oceanography based on Ocean City CTD during POLARSTERN cruise PS122. PANGAEA. DOI: https://doi.org/10.1594/PANGAEA.959964.

Toole, JM, **Krishfield, R**, **O'Brien, JK**, **Houk, AE**, **Cole, ST.** 2016. Ice-tethered profiler observations: Vertical profiles of temperature, salinity, oxygen, and ocean

velocity from an ice-tethered profiler buoy system [Dataset]. National Centers for Environmental Information. DOI: https://doi.org/10.7289/v5mw2f7x.

Uttal, T, **Curry, JA**, **McPhee, MG**, **Perovich, DK**, **Moritz, RE**, **Maslanik, JA**, **Guest, PS**, **Stern, HL**, **Moore, JA**, **Turenne, R**, **Heiberg, A**, **Serreze, MC**, **Wylie, DP**, **Persson, OG**, **Paulson, CA**, **Halle, C**, **Morison, JH**, **Wheeler, PA**, **Makshtas, A**, **Welch, H**, **Shupe, MD**, **Intrieri, JM**, **Stamnes, K**, **Lindsey, RW**, **Pinkel, R**, **Pegau, WS**, **Stanton, TP**, **Grenfeld, TC.** 2002. Surface heat budget of the Arctic Ocean. *Bulletin of the American Meteorological Society* **83**(2): 255–276. DOI: https://doi.org/10.1175/1520-0477(2002)083<0255:SHBOTA>2.3.CO;2.

Watkins, DM, **Persson, POG**, **Stanton, T**, **Solomon, A**, **Hutchings, JK**, **Haapala, J**, **Svensson, G.** 2024. Air-ice-ocean coupling during a strong mid-winter cyclone: Observing coupled dynamic interactions across scales. *Journal of Geophysical Research: Atmospheres* **129**(17). DOI: https://doi.org/10.1029/2024JD041057.

Woodgate, RA, **Weingartner, TJ**, **Lindsay, R.** 2010. The 2007 Bering Strait oceanic heat flux and anomalous Arctic sea-ice retreat. *Geophysical Research Letters* **37**(1). DOI: https://doi.org/10.1029/2009GL041621.

Yang, J. 2006. The seasonal variability of the Arctic Ocean Ekman transport and its role in the mixed layer heat and salt fluxes. *Journal of Climate* **19**(20): 5366–5387. DOI: https://doi.org/10.1175/JCLI3892.1.

Zhao, M, **Timmermans, M-L.** 2016. Vertical scales and dynamics of eddies in the Arctic Ocean's Canada Basin. *Journal of Geophysical Research: Oceans* **120**(12): 8195–8209. DOI: https://doi.org/10.1002/2015JC011251.

How to cite this article: Fang, Y-C, Rabe, B, Kuznetsov, I, Hoppmann, M, Tippenhauer, S, Regnery, J, He, H, Li, T. 2026. Upper-ocean variability in the Amundsen Basin of the Arctic Ocean during early winter: Insights from the MOSAiC expedition. *Elementa: Science of the Anthropocene* 14(1). DOI: https://doi.org/10.1525/elementa.2023.00095

Domain Editor-in-Chief: Jody W. Deming, University of Washington, Seattle, WA, USA

Guest Editor: Wieslaw Maslowski, Naval Postgraduate School, Monterey, CA, USA

Knowledge Domain: Ocean Science

Part of an Elementa Special Feature: The Multidisciplinary Drifting Observatory for the Study of Arctic Climate (MOSAiC)

Published: April 06, 2026 **Accepted:** December 26, 2025 **Submitted:** June 23, 2023

ELEMENTA Science of the Anthropocene

Elem Sci Anth is a peer-reviewed open access journal published by University of California Press.

OPEN ACCESS